이 학 석 사 학 위 논 문

Monte Carlo Simulation and Experimental Characterization of Tissue Equivalent Proportional Counter for Dosimetry of Neutron and Photon Fields

중성자 및 감마 선량 측정을 위한 조직등가 비례 계수기의 몬테카를로 전산모사와 실험

2018년 8월

서울대학교 융합과학기술대학원

융합과학부 방사선융합의생명 전공

Justin Malimban

A Thesis for the Degree of Master of Science

Monte Carlo Simulation and Experimental Characterization of Tissue Equivalent Proportional Counter for Dosimetry of Neutron and Photon Fields

중성자 및 감마 선량 측정을 위한 조직등가 비례 계수기의 몬테카를로 전산모사와 실험

August 2018

Program in Biomedical Radiation Sciences

Department of Transdisciplinary Studies

Graduate School of Convergence Science and Technology

Seoul National University

Justin Malimban

Monte Carlo Simulation and Experimental Characterization of Tissue Equivalent Proportional Counter for Dosimetry of Neutron and Photon Fields

지도교수 예성준

이 논문을 이학석사학위논문으로 제출함

2018 년 4 월

서울대학교 융합과학기술대학원

융합과학부 방사선융합의생명전공

Justin Malimban

저스틴의 석사학위논문을 인준함

2018 년 7 월

위 원 장 _____ 최희동 _____ (인)

부 위 원 장 _____ 예성준 _____ (인)

위 원 _____ 남욱원 _____ (인)

Monte Carlo Simulation and Experimental Characterization of Tissue Equivalent Proportional Counter for Dosimetry of Neutron and Photon Fields

by

Justin Malimban

A thesis submitted to the Department of Transdisciplinary Studies in partial fulfillment of the requirements for the Degree of Master of Science in Biomedical Radiation Sciences in the Graduate School of Convergence Science and Technology

Seoul National University

July 2018

Approved by the thesis committee:

Chairman: 최희동 H.D. Choi (인)

Vice Chairman: 예성준 Sung-Jun Ye (인)

Examiner: 남욱원 Uk-Won Nam (인)

ABSTRACT

Monte Carlo Simulation and Experimental Characterization of Tissue Equivalent Proportional Counter for Dosimetry of Neutron and Photon Fields

Justin Malimban

Program in Biomedical Radiation Sciences

Department of Transdisciplinary Studies

Graduate School of Convergence Science and Technology

Seoul National University

The Tissue Equivalent Proportional Counter (TEPC) is a radiation detector generally used for experimental microdosimetry. The TEPC offers a physical approach in measuring energy depositions in a microscopic volume by filling the gas cavity with a low-pressure gas. It allows observation of the behavior of

the patterns of energy distribution in the microscopic scale, which is critical in understanding the interaction of radiation especially to the sensitive structures of the cell. Over the last two decades, TEPCs of different shapes and sizes tailored to specific applications have been developed due to the growing interest in space exploration as well as particle beam therapies where various types of radiation contribute to the dose.

The purpose of this dissertation is to observe the response of the Benjamin-type TEPC developed by the Korea Astronomy and Space Science Institute (KASI) for mixed radiation fields. Experimental measurements were performed in order to evaluate its capability in measuring the microdosimetric spectra for a 2 μm-simulated site in a pure propane gas when irradiated with Cs-137 gamma and Cf-252 neutron sources. Furthermore, Monte Carlo (MC) modelling of the TEPC using the Geant4 simulation toolkit was also carried out to validate the experimental results and to evaluate its capability in reproducing the measured spectra.

The frequency-weighted lineal energy distribution ($yf(y)$) and dose-weighted lineal energy distribution ($yd(y)$) were constructed from both the simulation and experimental data. The frequency-mean lineal energy ($\bar{y}_F$) and dose-mean lineal energy ($\bar{y}_D$) were subsequently calculated. For the photon irradiation, the shape of the experimental spectrum was accurately predicted by the simulation when low lineal energy events were not considered. The difference in the measured and calculated $\bar{y}_F$ and $\bar{y}_D$ values for the photon case were 2.8% and 4%, respectively, when low lineal energy events were disregarded.

Similarly, the shape of the calculated spectra for the neutron irradiation was in overall agreement with the experimental one particularly in the region of the

neutron-induced peak. However, underestimation in the simulated spectra along the low lineal energy region was observed. Removal of the gamma region resulted in a satisfactory agreement between the measured and calculated $\bar{y}_F$ and $\bar{y}_D$ values within 5%. Although discrepancies were observed for the neutron case, the results in this work indicated that the simulation model based on the Geant4 toolkit successfully reproduced and predicted the experimental microdosimetric spectra with reasonable accuracy for both irradiation conditions.

Keywords: Tissue equivalent proportional counter, Lineal energy, Microdosimetry, Photon, Neutron

Student Number: 2016-27697

List of Tables

List of Figures

CONTENTS

Introduction

The tissue equivalent proportional counter (TEPC) is the standard instrument used for experimental microdosimetry [1]. The TEPC allows measurement of the single-event energy depositions in microscopic regions by filling the sensitive volume of the counter with very low-pressure gas of equal effective dimensions as cellular and subcellular targets [1, 2]. It offers a physical approach on the investigation of the spatial distribution of energy deposition events in microscopic volumes which is vital for understanding the mechanism of radiation damage [3].

The quantity obtained from measurements using the TEPC is the lineal energy (y) which is defined as the quotient of the energy imparted (ϵ) in a volume due to a single energy deposition event and the mean chord length ($\bar{l}$) of that volume [3]. The lineal energy is the stochastic analog of the linear energy transfer (LET) and is usually expressed in terms of keV/μm.

The lineal energy distributions obtained from TEPCs are useful particularly in predicting the relative biological effectiveness (RBE) of different types of radiation for equal absorbed doses [4]. This is extremely valuable for dosimetry in mixed radiation fields such as the space radiation environment, proton, ion beam and boron neutron capture therapy (BNCT) facilities. TEPCs have been proven to accurately measure the different dose components in these environments.

Thus, several studies dedicated mostly on the development and fabrication of TEPCs tailored to specific applications have been performed in the past as commercially-available ones are not always applicable. Depending on the radiation environment of concern, TEPCs of different shapes and sizes have been developed. For example, cylindrical mini-TEPCs which are capable of withstanding high flux proton and BNCT beams have been developed in the works of Cesari *et al*, De Nardo *et al* and Moro *et al* [5-7]. Microdosimetric measurements using these novel mini-TEPCs are particularly important as alternative radiotherapy modalities involving particle and neutron beams are becoming more popular. Furthermore, spherical TEPCs designed for dose monitoring in the International Space Station (ISS) were also described in the works of Moro *et al* [8] and Nam *et al* [9]. Before implementation of these detectors, characterization using different radiation fields are usually conducted beforehand to evaluate their performance.

Similarly, in this study, the response of the D60 TEPC developed and fabricated by the Korea Astronomy and Space Science Institute (KASI) was evaluated for photon and neutron fields. Comparison of the experimental data with Monte Carlo (MC) simulations was also facilitated in the present work. The microdosimetric spectra and microdosimetric quantities, frequency-mean lineal energy ($\bar{y}_F$) and the dose-mean lineal energy ($\bar{y}_D$), were used as a means of comparison between the measurements and calculations. The physical absorbed dose and the equivalent dose were also calculated from the experimental results for both the gamma and neutron irradiation conditions.

Material and Methods

2.1. Detector Geometry

The tissue equivalent proportional counter (TEPC) used in this study is a Benjamin-type spherical TEPC which was designed and developed by the Korea Astronomy and Space Science Institute (KASI). The cross-sectional illustration of the detector is shown in figure 1(a). The sensitive volume of the TEPC is 60 mm in diameter and is surrounded by a 3 mm thick cathode wall made of A150 tissue equivalent (TE) plastic. The stainless steel anode wire is 30 μm in diameter and is mounted axially along the central axis of the TEPC. An outer housing made of 1.5 mm thick aluminum was employed to create an air tight seal and protect the TEPC from electromagnetic interference. The detailed specifications of the detector are presented in table 1.

The TEPC was operated in sealed mode and the gas cavity was filled with pure propane gas at a density of 3.33×10^{-5} g/cm^3 calculated using equation 1

$$\rho_g = \rho_t \frac{d_t}{d_g} \qquad \textbf{Eq. 1}$$

where ρ_t is the density of tissue (1 g/cm^3), d_t is the simulated site size and d_g is the diameter of the gas cavity. A 2 μm diameter site size was arbitrarily chosen for the present work. The corresponding pressure (P) to this gas density was subsequently obtained using the expression below

$$P = \rho_g \frac{RT}{M}, \qquad \textbf{Eq. 2}$$

where R is the gas constant (62.365×10^3 cm^3·torr/mol·K), T is the temperature (293.15 K) and M is the molar mass of propane (44.1 g/mol). The calculated pressure of the propane gas was 13.9 torr.

It has to be noted that the type of gas used in this study is pure propane gas (C_3H_8) instead of propane-based tissue equivalent gas (C_3H_8-TE). Pure propane gas exhibits higher gas gain and longer stability as compared to propane-based TE gas which is particularly advantageous for sealed TEPCs [10]. Due to the difference in the ionization yields between C_3H_8 and C_3H_8-TE, the density of C_3H_8 must be reduced by 25% to get the same response for a particular tissue site size according to the work of Chiriotti *et al* [8, 10]. Therefore, a TEPC filled with C_3H_8 corresponding to a 2 μm simulated site size would yield the same number of ionizations as a 2.66 μm simulated site in C_3H_8-TE (equation 3). This indicates that a particle traversing the gas cavity will experience the same energy loss as when it is travelling a 2.66 μm diameter tissue site.

$$d_t = \frac{d_g \rho_g}{0.75 \times \rho_t} \qquad \textbf{Eq. 3}$$

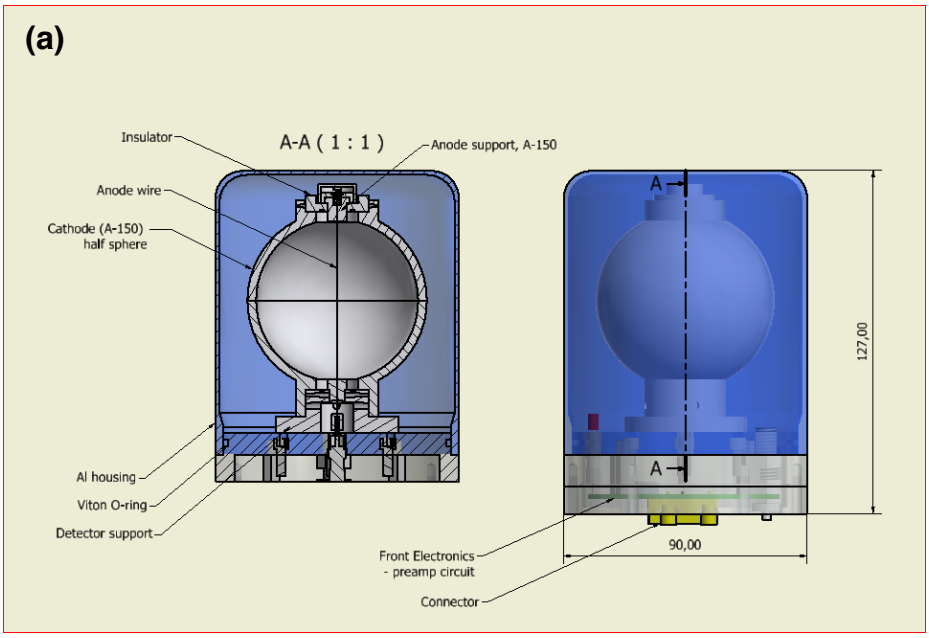

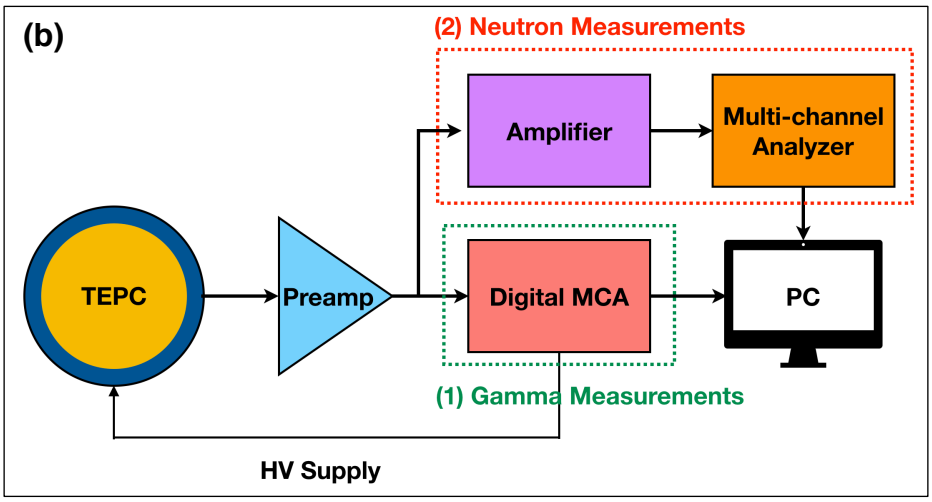

Figure 1. (a) Cross-sectional illustration of the D60 TEPC developed by the Korea Astronomy and Space Science Institute (Courtesy of Dr. Ukwon Nam of KASI) and (b) schematic diagram of the electronic chain for processing of the TEPC signal for photon (green) and neutron (red) measurements.

Table 1. Specifications of the D60 TEPC developed by the Korea Astronomy and Space Science Institute (KASI).

Parameters	Values
Diameter (mm)	60
Wall thickness (mm)	3
Simulated diameter in propane (μm)	2
Simulated tissue diameter (μm)	2.66
Mean chord length (μm)	1.77
Gas Pressure (torr)	13.9
Gas density (g/cm^3)	3.33×10^{-5}
Cavity Volume (cm^3)	113.10
Surface Area (cm^2)	136.85

2.2. Electronic Chain

The TEPC was operated at a voltage bias of -610V in pulse mode to record each energy deposition event. The charge collected in the gas cavity for each event is converted to a voltage pulse through a charge sensitive preamplifier (model A250, AMPTEK, Inc., Bedford, MA, USA). The preamplifier was connected close to the detector to minimize electronic noise. Different electronic set-ups were implemented for the photon and neutron measurements. For the photon measurement, the output from the preamplifier was sent to a dual digital multi-channel analyzer (model DT5780M, CAEN S.p.a, Viareggio, Italy) for shaping and conversion of analog to digital signals. The digital MCA was connected to a computer running the CAEN mc^2 Analyzer software for acquisition and plotting of the histogram data.

However, the neutron measurements cover a wide range of lineal energy that using a digital pulse processor affects the acquisition of data in the lower lineal energy region. Therefore, analog pulse processing method was used instead. The output signal from the preamplifier for the neutron measurement was sent to a shaping amplifier (Ortec-570, AMETEK, Inc., Oak Ridge, TN) which was connected to a multichannel analyzer (MCA8000D, AMPTEK, Inc., Bedford, MA). The data was acquired using the AMPTEK DppMCA software. The schematic diagram of the detector set up is illustrated in figure 1(b).

2.3. Photon Field Measurements

2.3.1. Experimental Measurements

The TEPC was exposed to a Cesium-137 gamma source (Eckert & Ziegler Isotope Products, Inc., Berlin, Germany) to observe its response to low LET events. The source emits 662 keV gamma rays, having an activity of 95.3 μCi at a reference date of December 15, 2012. The source was placed directly in front of the TEPC as shown in figure 2 and the irradiation was performed for 30 minutes.

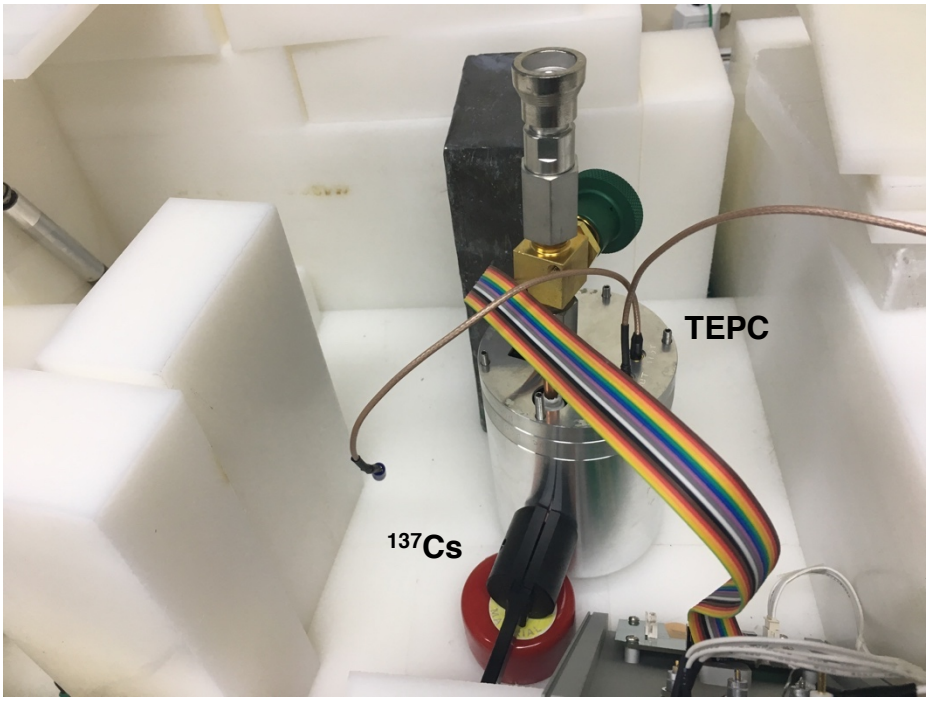

Figure 2. Irradiation set-up for the gamma characterization with the ^{137}Cs source placed directly in front of the TEPC.

2.3.2. Electron Edge Calibration

The calibration of the channels in terms of lineal energy for the photon measurement was carried out through the electron edge calibration method described in the work of Conte *et al* for cylindrical TEPCs [11] and in the work of Moro *et al* for spherical TEPCs [12]. The *electron edge* refers to a region in the microdosimetric spectrum of a photon beam wherein a sharp drop can be observed in the dose distribution owing to electrons traversing the longest chord of the sensitive volume (i.e., exact stoppers) [7, 11, 13]. Thereby, recording the maximum possible lineal energy.

In order to conduct the calibration, the dose distribution in $hd(h)$ was obtained using equation 4

$$h_i \cdot d(h_i) = \frac{n_i \cdot h_i^2}{\sum_i^N n_i \cdot h_i} \qquad \textbf{Eq. 4}$$

where h is the channel number, n is the number of counts and $d(h)$ is the dose probability density. Along the electron edge region, a fermi-like function given in equation 5 was fitted through least squares method to find parameters *A*, *B* and *C* which can be used to analytically calculate for the electron edge markers, h_{flex}, $h_{\delta\delta}$and h_{tC}, described in the work of Conte *et al* [11]. The three electron edge markers of interest are given in equation 6

$$h \cdot d(h) = \frac{A}{1 + e^{B \cdot (h - C)}} \qquad \textbf{Eq. 5}$$

$$h_{flex} = C; \qquad h_{\delta\delta} = \frac{\ln(2 + \sqrt{3})}{B} + C; \qquad h_{tC} = \frac{2}{B} + C \qquad \textbf{Eq. 6}$$

where h_{flex} is the channel where the inflection point occurred in the dose

distribution, $h_{\delta\delta}$ is the position of the maximum of the second derivative at the inflection point and h_{tC} is the intercept of the tangent line crossing the inflection point [11]. A Matlab script was written to perform the fitting to the experimental $hd(h)$ distribution and to calculate the electron edge marker values. The range of the channels considered in the fitting was adjusted to observe significant changes in the calculated values of the markers. The average values of the markers were taken for all considered intervals.

Typically, the lineal energy assigned to the h-value (i.e., channel) of the electron edge is done experimentally using an alpha source [11, 14]. However, in this study, the alpha calibration was not performed and the value assigned for the channel of the electron edge was the y-value calculated through Monte Carlo simulation in section 2.3.2. Therefore, the method described above was also implemented in the simulation results to calculate the electron edge markers in terms of lineal energy. However, instead of the $hd(h)$ distribution, the $yd(y)$ distribution was used to get the equivalent electron edge markers in lineal energy, y_{flex}, $y_{\delta\delta}$and y_{tC}.

2.3.3. Monte Carlo Simulation

The response of the TEPC to a pure gamma source was modelled using the Geant4 toolkit version 10.03.p01 [15]. The actual dimensions of the TEPC given in section 2.1 were implemented in the calculations. The ^{137}Cs source was modelled as an isotropic point source emitting 662 keV gamma rays placed in 15 mm away from the TEPC as shown in figure 3. The energy deposited per event was obtained using the primitive scorer *G4PSEnergyDeposit* for 1x10^{9}

histories. The deposited energy per event was later converted to the lineal energy by dividing it with the mean chord length as follows

$$y = \frac{\epsilon}{\bar{l}} \qquad \textbf{Eq. 7}$$

The mean chord length ($\bar{l}$) is defined as the average length of randomly-oriented chords in a volume [3]. For a spherical volume of diameter d irradiated by a uniform isotropic source, the mean chord length is mathematically expressed as

$$\bar{l} = \frac{2}{3}d \qquad \textbf{Eq. 8}$$

and is equal to 1.77 μm for a 2.66 μm simulated tissue site size [16].

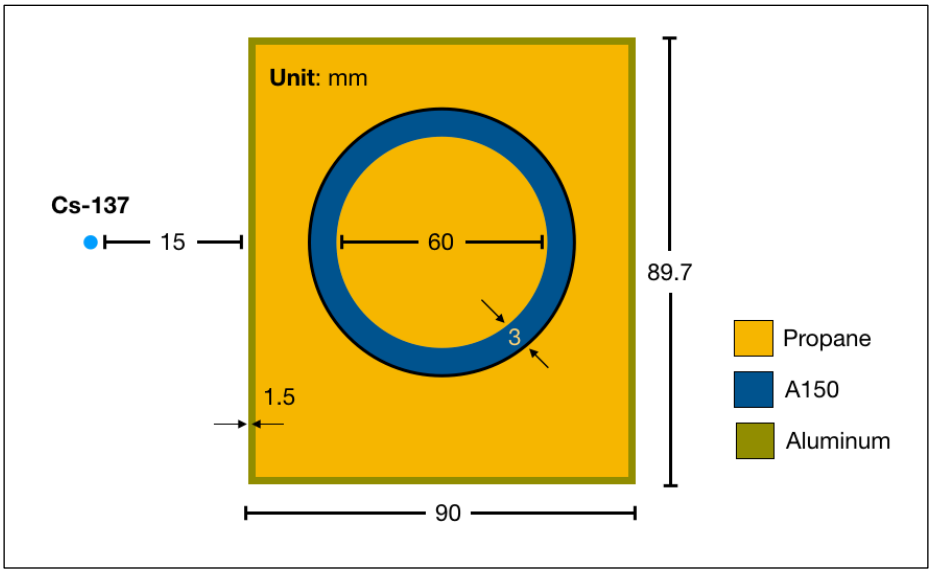

Figure 3. Schematic diagram of the simulation geometry using 662 keV monoenergetic gamma rays positioned 15 mm away from the surface of the aluminum case of the TEPC (not scaled).

2.4. Neutron Field Measurements

2.4.1. Experimental Measurements

Neutron measurements were also performed using a Californium-252 neutron source (model N-252) produced by Eckert & Ziegler. The ^{252}Cf cylindrical source was 3.2 mm long and has an active diameter of 1.6 mm. The active volume was encapsulated by Type 304L stainless steel with a length of 32.5 mm and a diameter of 9.4 mm. The activity of the source was 90 μCi at the reference date of December 1, 2013.

The source has an effective half-life of 2.645 years which decays 96.91% through alpha emission and 3.09% through spontaneous fission (SF), releasing both neutrons and gamma rays as shown in figure 4 [17, 18]. ^{252}Cf releases an average number of 3.78 neutrons and 7.98 gammas per spontaneous fission event [19, 20]. The average and the most probable neutron energy emitted by ^{252}Cf are 2.13 MeV and 0.70 MeV, respectively [19, 21, 22].

In the experimental set-up, the center of the source was positioned 125 mm away from the center of the TEPC and the exposure was performed for about 10 hours because of the low activity of the ^{252}Cf source. The source was held in place 285 mm from the ground by an aluminum holder with thickness of 1 mm as shown in figure 5.

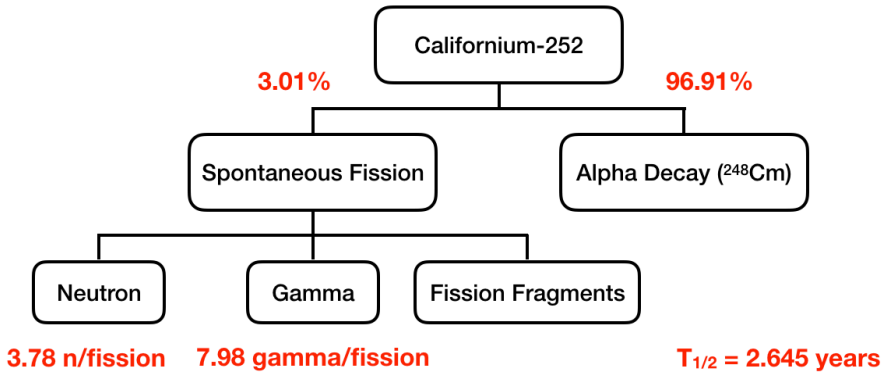

Figure 4. Decay scheme of Californium-252.

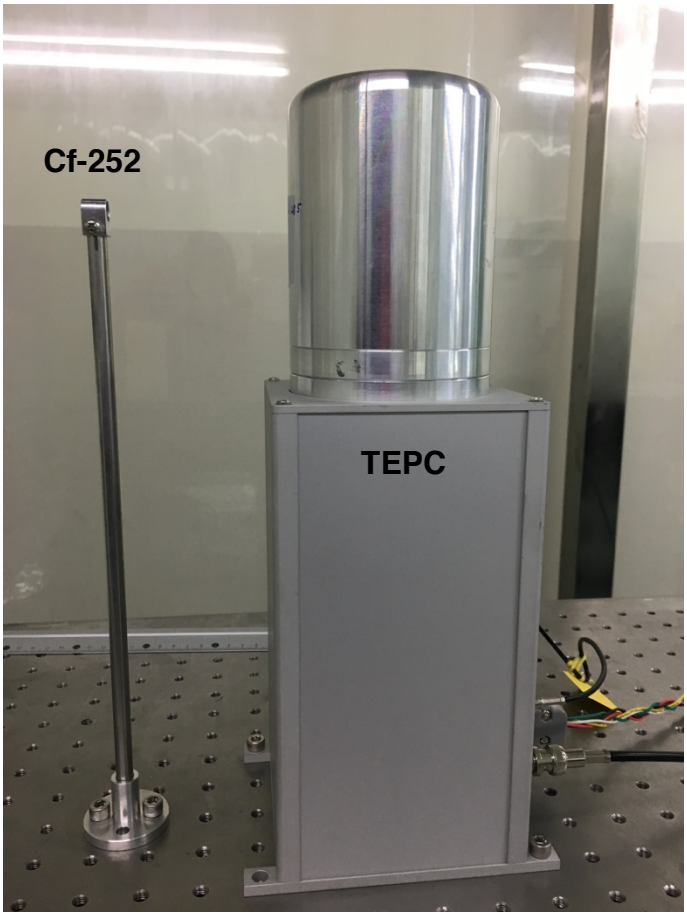

Figure 5. Irradiation set-up for the neutron measurement with the Cf-252 source positioned 125 mm away from the center of the TEPC. The source was placed in an aluminum holder with thickness of 1 mm elevated 285 mm from the ground.

2.4.2. Proton Edge Calibration

The experimental neutron pulse height spectrum was calibrated in terms of lineal energy using the proton edge calibration method. Similar with the electron edge, the *proton edge* refers to the maximum lineal energy deposited by protons that traversed the main chord of the gas cavity [23, 24]. This reference point is also characterized by a sharp drop in the number of counts in the spectrum and is smoother and much more noticeable in the dose distribution than the electron edge.

The same general procedure but with a few modifications in the electron edge calibration method described in section 2.3.2 was employed for the proton edge calibration. Although measurements were performed for 10 hours, the neutron spectrum acquired from the TEPC had relatively low counting statistics and the experimental data was rather scattered as can be observed in figure 6(a). Therefore, efforts to smooth the spectrum was first performed before fitting the fermi-like function.

Instead of using the channels in plotting the $hd(h)$ spectrum, the corresponding pulse amplitude in mV was used to construct the dose distribution. This is to allow logarithmic re-binning in order to further smoothen the data. The channels were first related to the pulse amplitude through the calibration equation

$$y_i\ [mV] = a + b \cdot x_i\ [channel] \qquad \textbf{Eq. 9}$$

where a = -8.84416 and b = 9.75905. Then, the calibrated pulse height spectrum in terms of mV was redistributed in a logarithmic fashion with the x-axis having

50 equally-spaced logarithmic bins per decade as shown in figure 6(b). A separate Matlab script was created to perform the logarithmic re-binning of the data. Detailed information on the process of re-binning can be found in the work of Motisi [25]. It also has to be noted that same notation, *h*, was used for the channels and the pulse amplitude in mV for this study.

Similarly, a fermi-like function was then fitted to the logarithmically re-binned spectrum to acquire the proton edge markers in mV. Same fitting was done to the simulated spectrum to acquire the corresponding proton edge markers in terms of lineal energy and relate them with the experimental markers. The fitting was done at different intervals and the average values were taken.

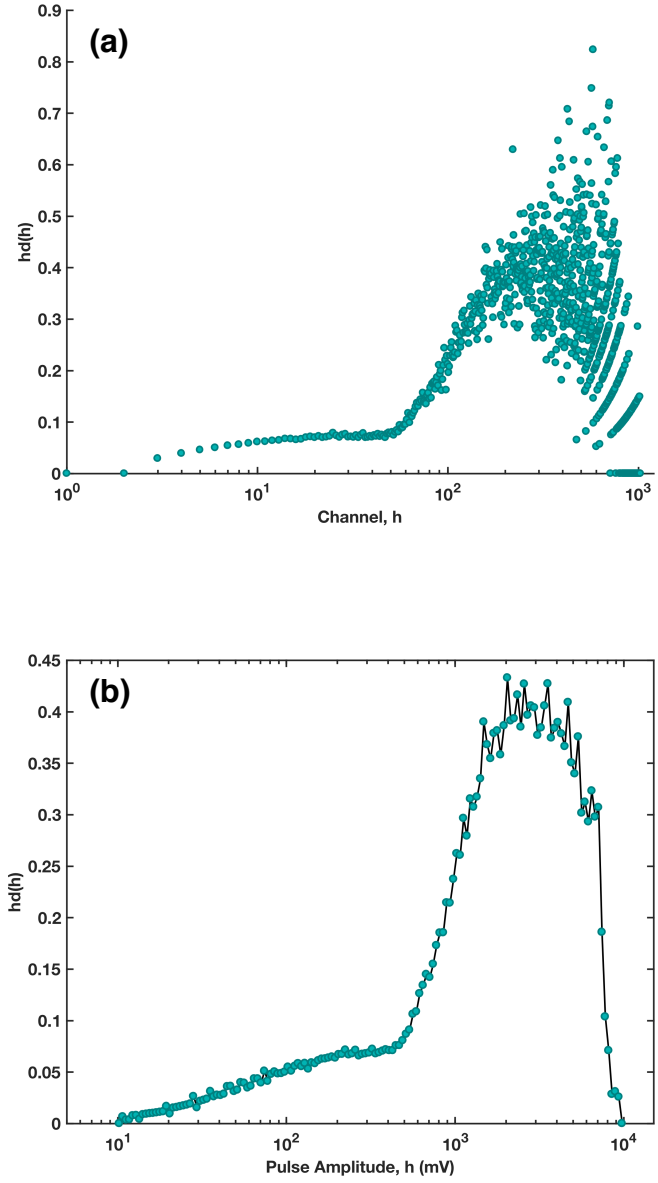

Figure 6. (a) Dose distribution in terms of channels and (b) calibrated dose distribution in terms of pulse amplitude in mV redistributed to 50 equally-spaced logarithmic bins per decade.

2.4.3. Monte Carlo Simulation

Similar with the gamma simulation, the performance of the TEPC when exposed to a neutron source was also evaluated through MC simulations using Geant4 toolkit version 10.03.p01 [15]. In order to reduce the calculation time, the entire simulation set-up was divided into two parts: (a) Californium-252 source modelling and (b) TEPC response modelling. The schematic diagrams of the simulation set-up of each part are shown in figures 7 and 8, respectively.

2.4.3.1. Californium-252 Modelling

The californium source (model N-252) produced by Eckert and Ziegler Isotopes Products was modelled as shown in figure 7(a) (refer to zoomed part). The actual dimension of the ^{252}Cf source was employed in the simulation. The isotopic composition of the source was ignored and the source was considered to be uniformly distributed within the cylindrical volume made of palladium with an isotropic emission along the 4π direction.

The Lawrence Livermore National Laboratory (LLNL) fission model was integrated in Geant4 to sample the neutron and photon energy distributions produced from the spontaneous fission of ^{252}Cf [26]. This is a data-driven model that implements correct neutron and gamma multiplicities and energy distributions which were found to be consistent with the Evaluated Nuclear Data File (ENDF/B-VII). Activation of this model overrides the built-in fission library of geant4 which has been found to produce inaccurate fission products [27, 28].

The neutron energy distribution of most fission spectra is sampled and can

be accurately represented by the Watt distribution [26, 27]. To validate the neutron spectrum produced using the LLNL fission library, the neutron energy spectrum for ^{252}Cf was also sampled from the Watt fission spectrum for spontaneous fission given in equation 10

$$f(E) \propto e^{-\frac{E}{a}} \cdot \sinh\left(\sqrt{Eb}\right) \qquad \textbf{Eq. 10}$$

where a and b are the parameters determined from fitting the Watt formula to the measured fission spectrum data (i.e., 0.847458 and 1.03419, respectively) and E is the neutron energy in MeV [26]. The energy distribution along the surface of the active volume was recorded for neutrons produced by both the LLNL fission model and the Watt fission spectrum and their distributions were subsequently compared.

After the validation, the phase space files were recorded at the surfaces of the stainless steel capsule and the aluminum holder to observe their effect on the neutron and gamma energy spectra. The phase space file contained the coordinates, directional cosines, kinetic energy and radiation type of each particle crossing the surface. Then, the phase space file was also recorded for all particles traversing through a 100 mm × 100 mm square plane positioned 80 mm away from the center of the source as shown on figure 7. This phase space file would serve as the source for the succeeding TEPC simulation to increase the number of hits in the gas cavity.

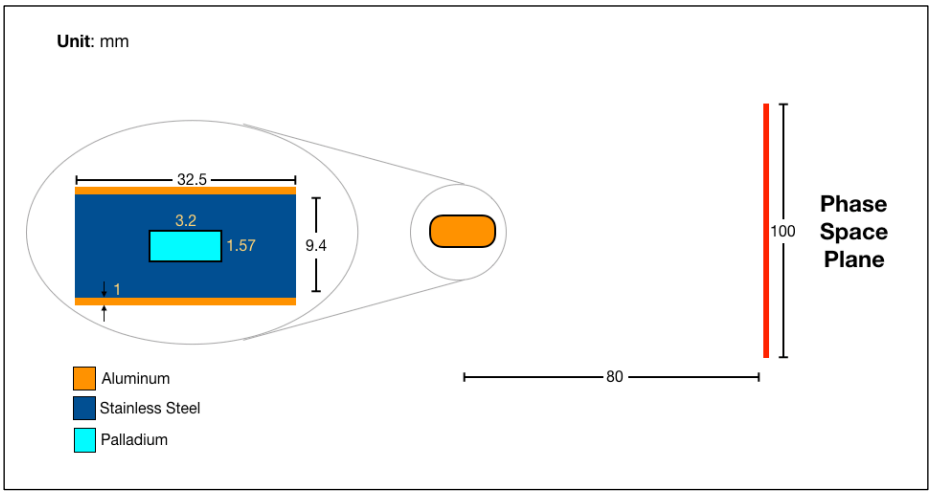

Figure 7. Schematic diagram of the simulation geometry for the ^{252}Cf neutron source. The phase space file to be used as the source for the succeeding TEPC simulation was acquired for a 100 mm × 100 mm square plane 80 mm away from the source. The zoomed portion shows the detailed specifications of the neutron source.

2.4.3.2. TEPC Modelling

Simulations modelling the response of the TEPC to the ^{252}Cf beam was performed using the phase space file acquired from section 2.4.3.1 as the source. The actual dimension of the TEPC as described in section 2.1 was implemented for the calculations. The elemental compositions of the materials used in the simulation are presented in table 2. The pre-packaged physics list QGSP_BIC_HP was implemented for the TEPC simulation. In this physics list, the neutron transport for energies below 20 MeV down to thermal energies is handled by the data driven High Precision (HP) model which was derived largely from the Evaluated Nuclear Data File/B version VII.1 (ENDF/B-VII.1).

The event-by-event energy deposition in the gas cavity was scored using the concrete primitive scorer G4PSEnergyDeposit. In addition to the total energy deposition scoring, two filters were also created to separately account for the gamma and neutron contributions. The *G4UserTrackingAction*, which stores the track history of the generated of particles, was implemented in the filters to identify the mother particle of each particle that deposited their energy in the sensitive volume. This allows for the separate scoring of gamma and neutron events. The total, neutron and gamma energy distributions were each recorded separately in a text file and were later converted to the lineal energy by dividing each energy deposition by the mean chord length ($\bar{l}$).

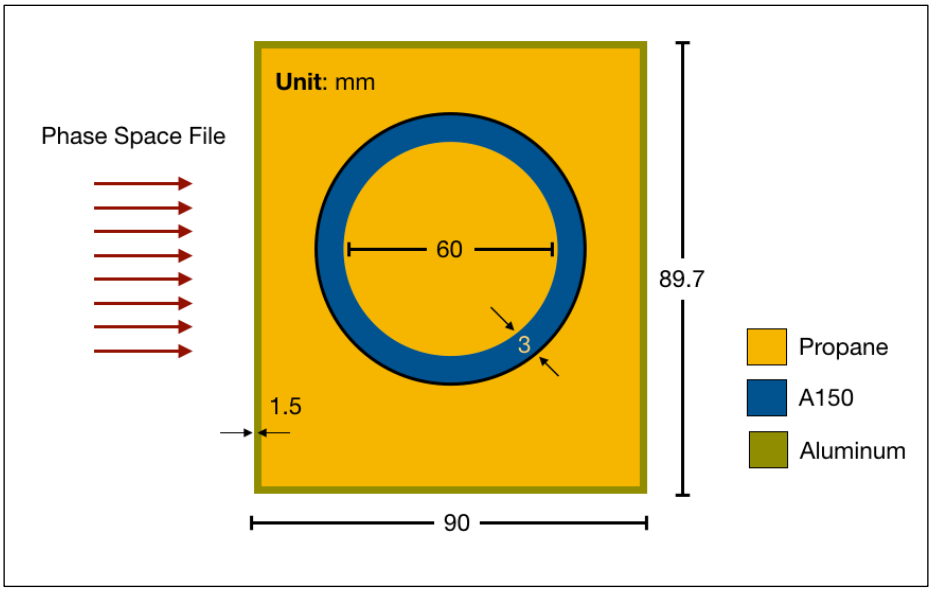

Figure 8. Schematic diagram of the simulation set-up for the TEPC modelling using the phase space files obtained from the previous simulation as the source.

Table 2. Elemental composition of A150 tissue equivalent (TE) plastic [29] and propane gas (taken from the National Institute of Standards and Technology) expressed in terms of percentage weight.

Material	H	C	N	O	F	Ca
A150	10.2	76.8	3.6	5.9	1.7	1.8
Propane	18.3	81.7	-	-	-	-

2.4.4. Data Analysis

The acquired frequency distribution, $f(y)$, from the experiment and simulation describes the occurrence of lineal energy events in the TEPC and is also referred to as the lineal energy distribution. The average of this distribution is referred to as the *frequency-mean lineal energy* ($\bar{y}_F$) and is derived from the following expression

$$\bar{y}_F = \int_0^\infty y f(y) \cdot dy \qquad \textbf{Eq. 11}$$

The $\bar{y}_F$ represents the mean lineal energy recorded by the TEPC.

From the frequency distribution, the dose distribution, $d(y)$, can be derived through equation 12

$$d(y) = \frac{y f(y)}{\bar{y}_F} \qquad \textbf{Eq. 12}$$

This distribution indicates the fraction of the absorbed dose associated with certain values of lineal energies. The average of this distribution is the *dose-mean lineal energy* ($\bar{y}_D$) given the equation below

$$\bar{y}_D = \int_0^\infty y d(y) \cdot dy = \frac{1}{\bar{y}_F} \int_0^\infty y^2 f(y) \cdot dy \qquad \textbf{Eq. 13}$$

which represents the mean lineal energy that contributed to the dose.

These $f(y)$ and $d(y)$ distributions acquired from microdosimetric measurements usually span a broad range of lineal energies, typically covering several orders of magnitude. Presentation of these distributions in the linear scale do not aid in the interpretation of data. Thus, as a convention, the $f(y)$ and $d(y)$ distributions are usually plotted on a logarithmic scale of y. The raw

data is then redistributed to equally-spaced logarithmic bins to improve the presentation of data.

To maintain the normalization of the distributions even when plotted in the logarithmic scale, the $f(y)$ and $d(y)$ distributions were transformed to $yf(y)$ and $yd(y)$ distributions through the expressions below

$$\int_0^\infty f(y) \cdot dy = \int_0^\infty yf(y) \cdot d(\ln y) \approx \frac{\ln(10)}{B} \sum_{i=0}^{\infty} y_i f(y_i) = 1 \quad \textbf{Eq. 14}$$

$$\int_0^\infty d(y) \cdot dy = \int_0^\infty yd(y) \cdot d(\ln y) \approx \frac{\ln(10)}{B} \sum_{i=0}^{\infty} y_i d(y_i) = 1 \quad \textbf{Eq. 15}$$

where B is the number of bins per decade. In this study, 50 equally-spaced logarithmic bins per decade was chosen. The $yf(y)$ and $yd(y)$ distributions are still the frequency and dose distributions but are based on the logarithmic scale. Throughout this document, the $yf(y)$ and $yd(y)$ distributions would be referred to as the frequency-weighted and dose-weighted lineal energy distributions, respectively. A Matlab script was written to facilitate the graphical presentation of the raw data and the calculation of microdosimetric quantities. Detailed information on the presentation of the microdosimetric spectrum can be found in the Appendix B of ICRU Report 36 [3].

The physical absorbed dose and the dose equivalent for both irradiation conditions were also calculated in this study. The absorbed dose (D) is given by the expression below

$$D = (1.602 \times 10^{-13}\ Gy/keV) \cdot \frac{\sum_{i=1}^{n} y_i \cdot f(y_i) \cdot \bar{l}}{\rho \cdot \forall} \quad \textbf{Eq. 16}$$

where n is the total number of bins, y_i is the midpoint of the ith lineal energy bin, $f(y_i)$ is the number of events in the ith bin, $\bar{l}$ is the mean chord length, ρ is the density of the gas and $\forall$ is the volume of the gas cavity. The dose equivalent (H) can be subsequently calculated using equation 17

$$H = D \cdot \bar{Q} \qquad \textbf{Eq. 17}$$

where $\bar{Q}$ is the average quality factor derived from the given expression

$$\bar{Q} = \frac{\sum_{i=1}^{n} Q(y_i) \cdot y_i \cdot f(y_i)}{\sum_{i=1}^{n} y_i \cdot f(y_i)} \qquad \textbf{Eq. 18}$$

$Q(y_i)$ is assumed to be equal to the quality factor $Q(L)$ given in ICRP 60 [30] wherein

$$Q(L) = \begin{cases} 1 & L < 10\ keV/\mu m \\ 0.32L - 2.2 & 10 \leq L \leq 100\ keV/\mu m \\ \dfrac{300}{\sqrt{L}} & L > 100\ keV/\mu m \end{cases} \qquad \textbf{Eq. 19}$$

Results

3.1. Response to a Photon Field

3.1.1. Experimental Results

Figure 9(a) shows the raw pulse height distribution acquired from exposure to ^{137}Cs. The measurement registered a total of 694,258 counts. The raw pulse height distribution was transformed to the dose distribution as a function of the channel (h) using equation 5 as shown in figure 9(b). The constructed dose distribution was subsequently used to identify at which channels the electron edge markers occurred to be used for calibration.

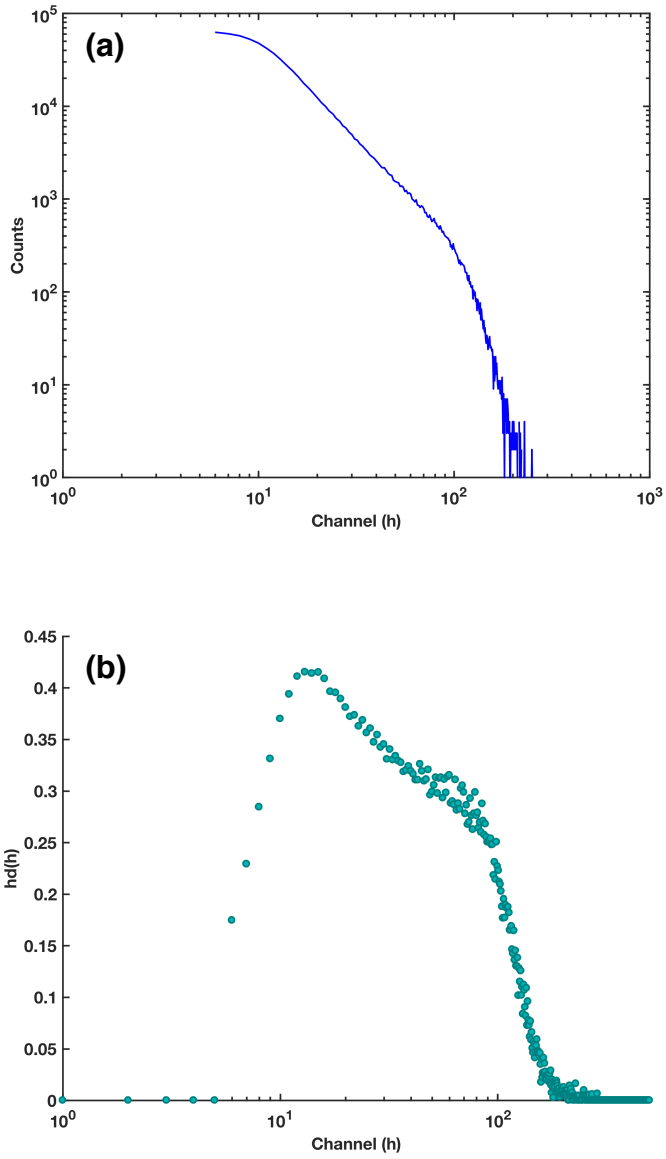

Figure 9. (a) Raw pulse height distribution due to the ^{137}Cs gamma source and (b) constructed dose distribution as a function of channel (*h*) for use in the electron edge calibration.

3.1.2. Simulation Results

Figures 10(a) and 10(b) show the frequency-weighted, $yf(y)$, and the dose-weighted, $yd(y)$, lineal energy distributions acquired through Monte Carlo simulation for the ^{137}Cs. Lineal energy values down to 0.01 keV/μm were recorded for both spectra. It can be observed that depositions from gamma rays produced by ^{137}Cs were composed of low lineal energy events up to 12.6 keV/μm. This is because the electrons produced by gamma rays which are responsible for the energy depositions have low LET. This behavior has been demonstrated already by several previous experimental studies with the electron edge occurring between 10 to 15 keV/μm [10-13]. The simulated $yd(y)$ spectrum was used to identify lineal energy values of the electron edge markers for the calibration of the experimental results.

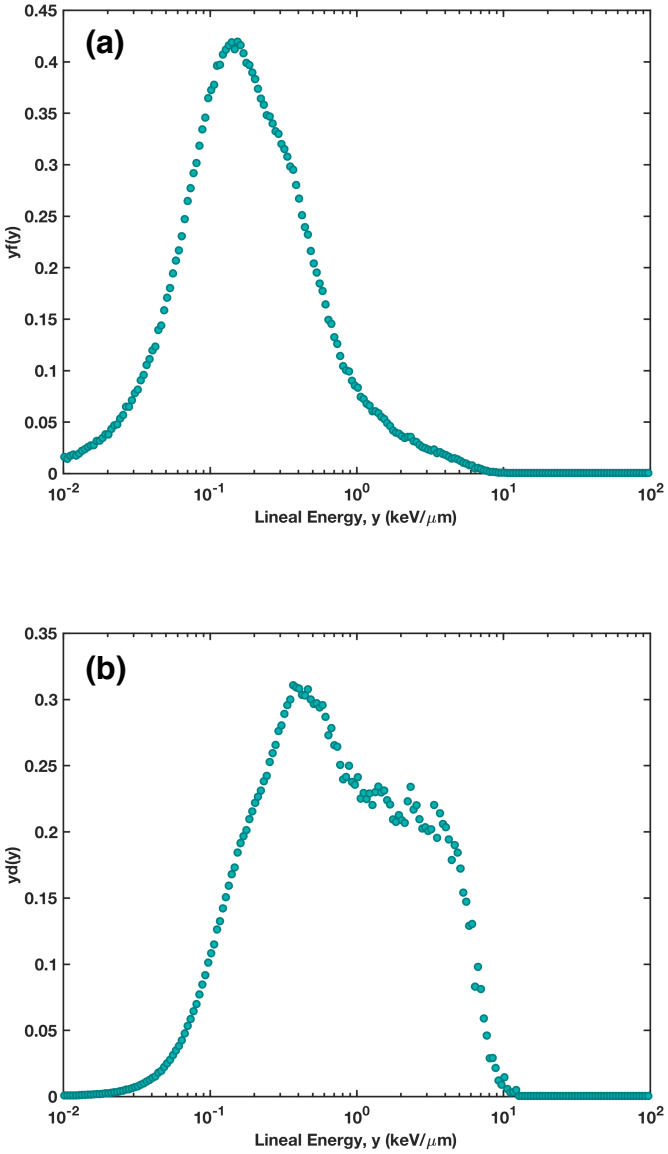

Figure 10. (a) Frequency-weighted and (b) dose-weighted lineal energy spectra obtained from MC simulation for 662 keV monoenergetic gamma source.

3.1.3. Electron Edge Calibration

The calibration of the raw pulse height spectrum was conducted through the electron edge self-calibration method. In this method, three markers in the dose distribution were identified at which a well-defined equivalent lineal energy value can be associated. Figures 11(a), (b), (c) and (d) show the fitted curve to the experimental data starting from channels 60, 70, 80 and 90, respectively. The corresponding h_{Flex}, $h_{\delta\delta}$ and h_{tC} values for each interval calculated from the fitting are presented in table 3.

The average values for the markers were rounded up to whole numbers and were assumed to be the h_{Flex}, $h_{\delta\delta}$ and h_{tC}values for calibration. The standard deviations for the markers obtained from the experimental data were also calculated and are also presented in table 3. h_{tC} recorded the lowest standard deviation among the three markers at 0.69 while h_{Flex} registered the largest at 2.2. The work of Conte *et al* also indicated that among the three electron edge markers, the h_{tC} marker is the most invariant with the fitting intervals [11]. Thus, the h_{tC} marker was chosen for calibration of the gamma microdosimetric spectrum in this study.

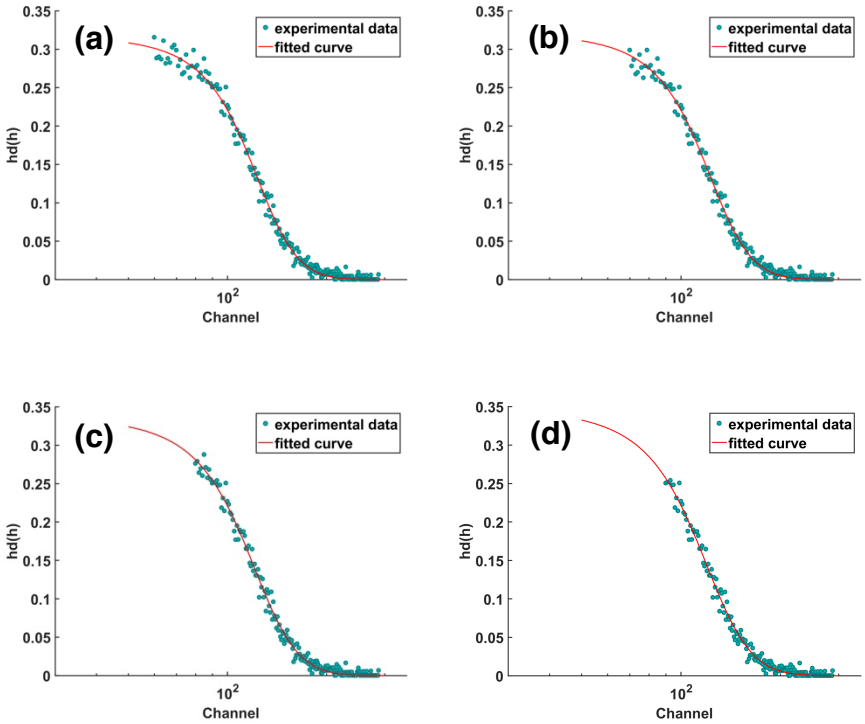

Figure 11. Fermi fit to the $hd(h)$ distribution at different channel intervals starting from (a) channel 60, (b) channel 70, (c) channel 80 and (d) channel 90 for the gamma irradiation.

Table 3. Experimental electron edge markers obtained at different channel intervals for the gamma irradiation.

Interval	h_{Flex}	$h_{\delta\delta}$	h_{tC}
60 ~ 2048	116.2	142.9	156.8
70 ~ 2048	115.6	142.7	156.8
80 ~ 2048	113.0	141.3	156.0
90 ~ 2048	111.5	141.8	156.2
Average	**114**	**142**	**156**
Standard Deviation	**2.2**	**1.2**	**0.69**

The same fitting method was employed for the simulated $yd(y)$ spectrum to acquire the electron edge markers in terms of lineal energy. Figures 12(a), (b), (c) and (d) illustrate the curve fitting to the simulated $yd(y)$spectrum at lineal energy intervals starting from 2, 3, 4 and 5 keV/µm, respectively. Table 4 presents the resulting y_{Flex}, $y_{\delta\delta}$ and y_{tC} values for all the considered fitting intervals as well as their average values and standard deviations. Since the h_{tC}marker was chosen for calibration, the value of y_{tC}which is 8.47 keV/µm was assigned to channel 156. This resulted to a calibration factor of 0.0543 keV/µm per channel and a detection range from 0.27 keV/µm to 111.2 keV/µm.

$$y_{calib(\gamma)} = \frac{y_{tC}}{h_{tC}} = \frac{8.47\ keV/\mu m}{channel\ 156} = 0.0543\ keV/\mu m \cdot channel \quad \textbf{Eq. 20}$$

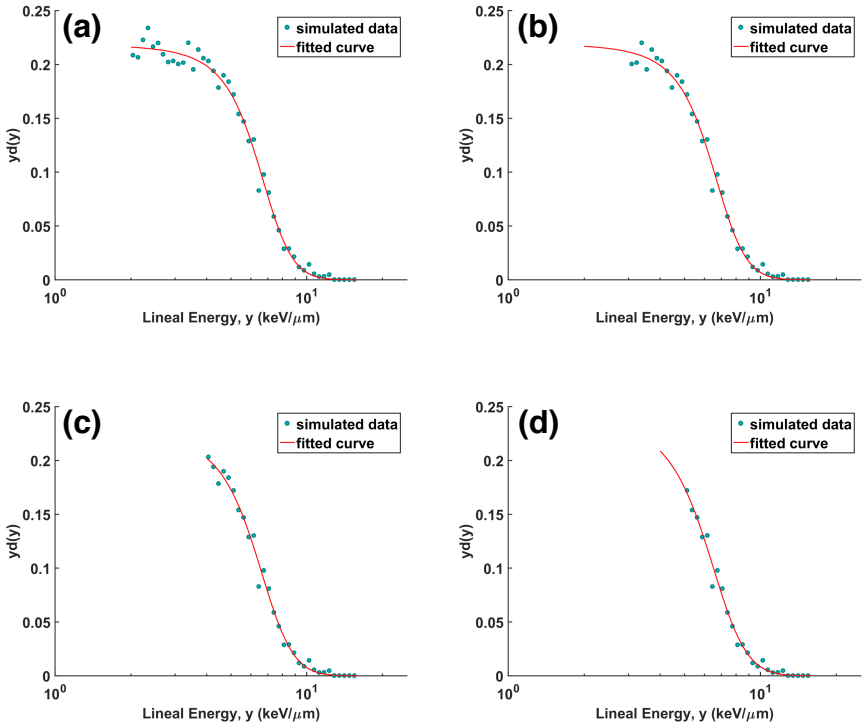

Figure 12. Fermi fit to the simulated $yd(y)$ distribution at different lineal energy intervals starting from (a) 2 keV/μm, (b) 3 keV/μm, (c) 4 keV/μm and (d) 5 keV/μm for the gamma irradiation.

Table 4. Simulated electron edge markers at different lineal energy intervals for the gamma irradiation.

Interval	y_{Flex}	$y_{\delta\delta}$	y_{tC}
2 ~ 111.2	6.37	7.76	8.48
3 ~ 111.2	6.36	7.75	8.48
4 ~ 111.2	6.25	7.72	8.49
5 ~ 111.2	6.09	7.63	8.44
Average	**6.27**	**7.72**	**8.47**
Standard Deviation	**0.13**	**0.06**	**0.02**

3.1.4. Experiment and Simulation Comparison

Figure 13(a) shows the comparison of the experimental and simulated $yd(y)$ spectrum for ^{137}Cs. At lineal energies less than 0.56 keV/μm, large discrepancies between the experimental and simulation results can be observed. This can be attributed to the detection limitations of the TEPC which cause some events to not be counted throughout the measurement period.

The frequency-mean lineal energy ($\bar{y}_F$) for the simulation obtained for the whole lineal energy range was lower as compared with the experimental $\bar{y}_F$. This was due to a larger number of low lineal energy events recorded for the simulation. This resulted in a 22.1% difference between the experimental and simulated $\bar{y}_F$. However, the difference in the number of low y-events had lesser effect in the $\bar{y}_D$ as they do not contribute significantly on the dose. This was demonstrated by the 7.9% difference between the simulated and experimental $\bar{y}_D$.

To achieve a much more comparable spectra, lineal energy events below 1 keV/μm were disregarded for both the experimental and simulation results. The comparison of the newly reconstructed experimental and simulated spectra is presented in figure 13(b). The $\bar{y}_F$ and $\bar{y}_D$ values were also recalculated and are given in table 6. Upon removal of low lineal energy events, the discrepancies between the experimental and simulated $\bar{y}_F$ and $\bar{y}_D$ were reduced to 3.2% and 4.0%, respectively. A comparable agreement can also be observed in the reconstructed $yd(y)$ spectra.

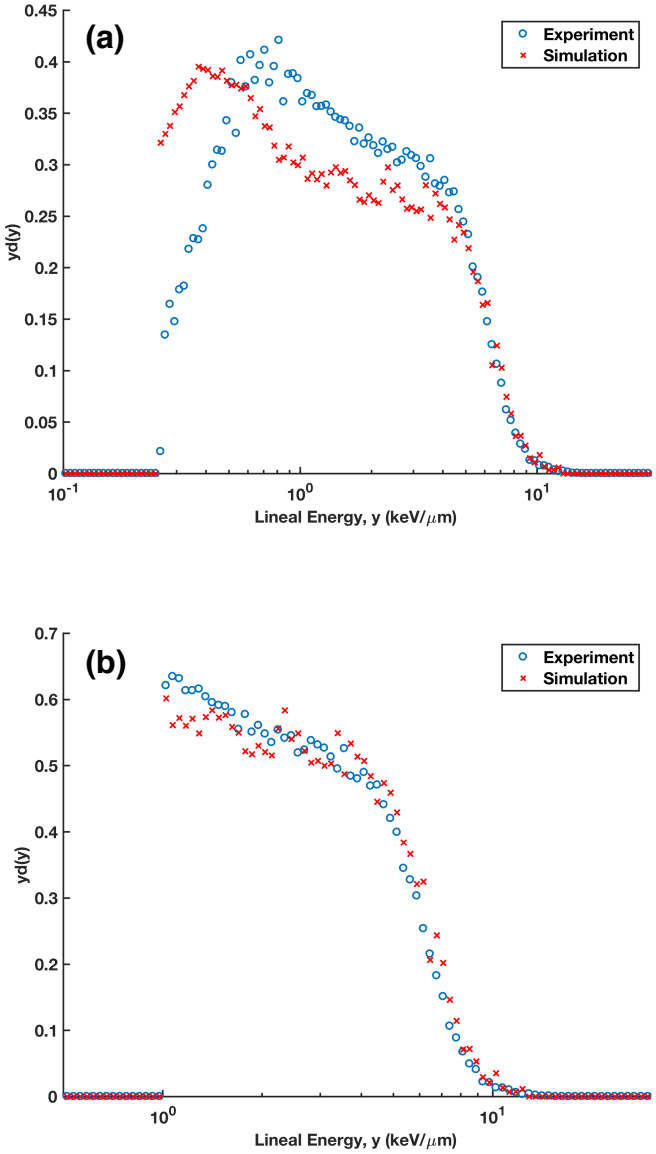

Figure 13. (a) Comparison of the experimental and simulated $yd(y)$ spectra for the whole lineal energy range and (b) reconstructed $yd(y)$ spectra without the contributions from lineal energies below 1 keV/μm.

Table 5. Experimental and simulated $\bar{y}_F$ and $\bar{y}_D$ values for the whole lineal energy range and their corresponding percent errors for the gamma irradiation.

Parameter	Experiment (keV/μm)	Simulation (keV/μm)	Percent Error (%)
$\bar{y}_F$	0.94	0.77	22.1
$\bar{y}_D$	1.92	1.78	7.9

Table 6. Experimental and simulated $\bar{y}_F$ and $\bar{y}_D$ values for the reconstructed spectrum considering only contributions above 1 keV/μm for the gamma irradiation.

Parameter	Experiment (keV/μm)	Simulation (keV/μm)	Percent Error (%)
$\bar{y}_F$	2.11	2.18	3.2
$\bar{y}_D$	2.86	2.98	4.0

3.2. Response to a Neutron Field

3.2.1. Experimental Results

Figure 14(a) shows the raw counts per channel recorded for the neutron measurements. This pulse height spectrum was calibrated in terms of the pulse amplitude in mV as illustrated in figure 14(b). The calibration in mV covered a range of pulse amplitudes from 0.92 mV to 9984.4 mV. This calibrated pulse height spectrum was used to construct the $hd(h)$ distribution shown in figure 6(b) which was subsequently used for the re-calibration of the experimental data in terms of lineal energy.

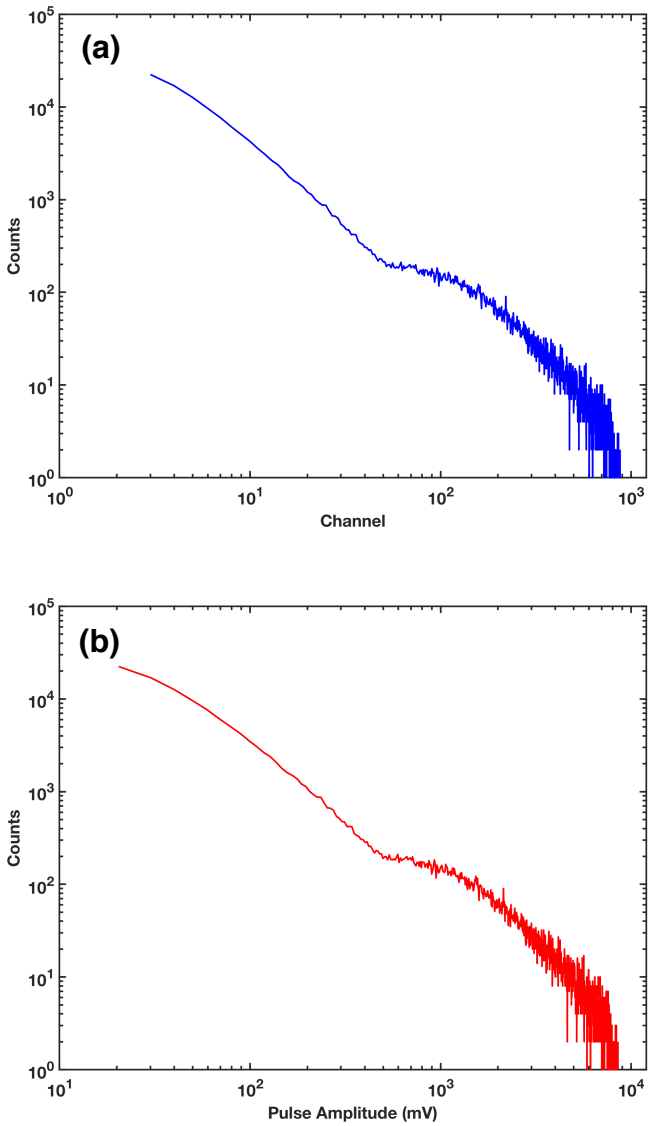

Figure 14. (a) Raw pulse height distribution and (b) calibrated pulse height distribution in mV for the neutron measurement.

3.2.2. Simulation Results

3.2.2.1. ^{252}Cf Neutron and Gamma Spectra

The simulated ^{252}Cf neutron and gamma spectra produced using the LLNL fission model is illustrated in figure 15. The model produced twice as much gamma rays as neutrons. To verify the simulated neutron spectrum, it was compared with the energy distribution sampled from the Watt fission spectrum. The ^{252}Cf spontaneous fission energy spectra produced from the LLNL fission model showed similar profiles and were found to be generally consistent with the Watt fission spectrum as illustrated in figure 16. Subtle differences can be observed which can be attributed to the nature of the sampling method employed. Nevertheless, the two spectra showed good agreement in their overall shape and energy range. Similar validation was also employed in the previous work of Tan *et al* wherein the energy distribution of fission neutrons generated by the LLNL fission model for ^{235}U was also compared and was found to be consistent with the Watt fission spectrum [28].

However, due to difficulty in finding references for the gamma spectrum produced by ^{252}Cf, the same validation as with neutrons was not performed for gamma. Instead, the average neutron and gamma energies were compared with existing published data as presented in table 7. The average neutron and gamma energy for the simulation were 2.12 MeV and 0.90 MeV, respectively. According to published data, the average neutron energy is 2.13 MeV [19] while the average gamma energy is 0.87 MeV [31].

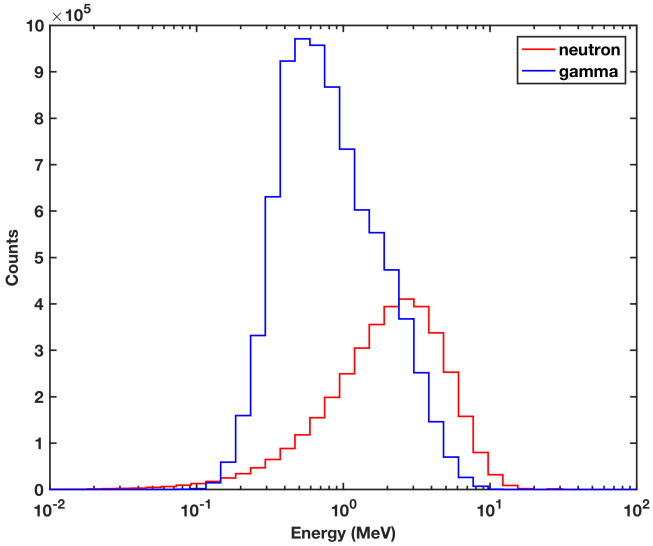

Figure 15. Neutron and gamma spectra produced using the LLNL fission model.

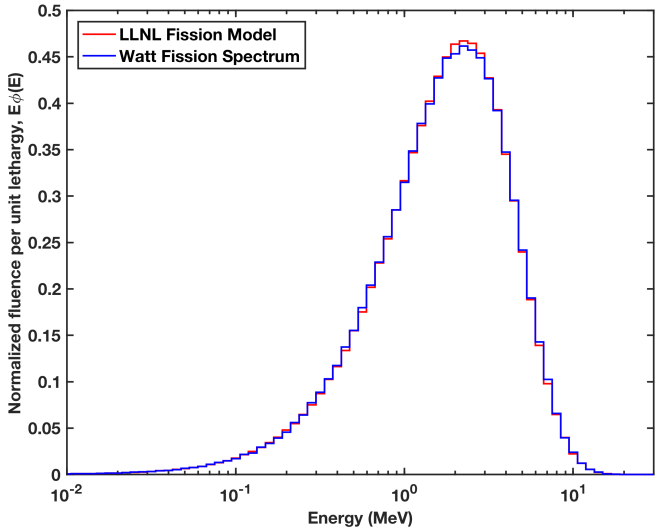

Figure 16. Comparison of the bare ^{252}Cf neutron energy distribution obtained using the LLNL fission model (red) and the Watt fission spectrum (blue).

Table 7. Simulated and published average neutron and gamma energies for ^{252}Cf.

	Simulation in this study (MeV)	**Published Data (MeV)**	**Percent Error (%)**
Neutron	2.12	2.13 [19]	0.5
Gamma	0.90	0.87 [31]	3.5

Furthermore, the phase space files were also recorded along the surface of the stainless steel capsule and aluminum holder and were compared with the bare source to assess changes on the neutron and gamma spectra. As shown in figure 17(a), compared with the bare source, the capsulated neutron spectrum is slightly shifted to lower neutron energies primarily due to thermalization of neutrons. However, the presence of the aluminum holder did not cause further drastic changes in the spectrum and was found to be almost similar with the capsulated neutron spectrum. The same behavior can be observed for the gamma spectra as illustrated in figure 17(b).

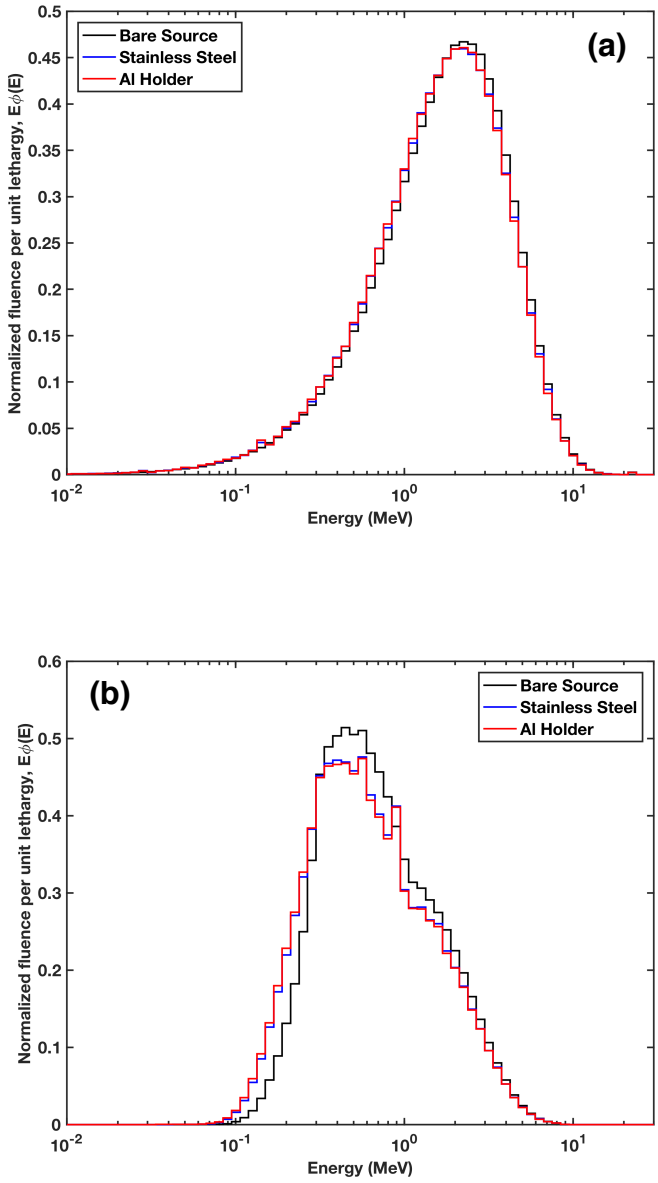

Figure 17. Comparison of the (a) neutron and (b) gamma distribution along the bare source (black), stainless steel capsule (blue) and aluminum holder (red).

The neutron and gamma spectra obtained from a 100 mm x 100 mm square plane 80 mm away from the center of the source (i.e., phase space file used as source in the succeeding TEPC simulation) were also compared with the bare neutron and gamma spectra, respectively. As shown in figure 18(a), the neutron spectrum recorded in the phase space plane is very similar with the bare neutron spectrum and is slightly shifted to the left to lower neutron energies. On the other hand, the opposite behavior was observed for the gamma rays as the gamma spectrum was shifted to higher energies as shown in figure 18(b) which was caused by attenuation of low energy gamma rays.

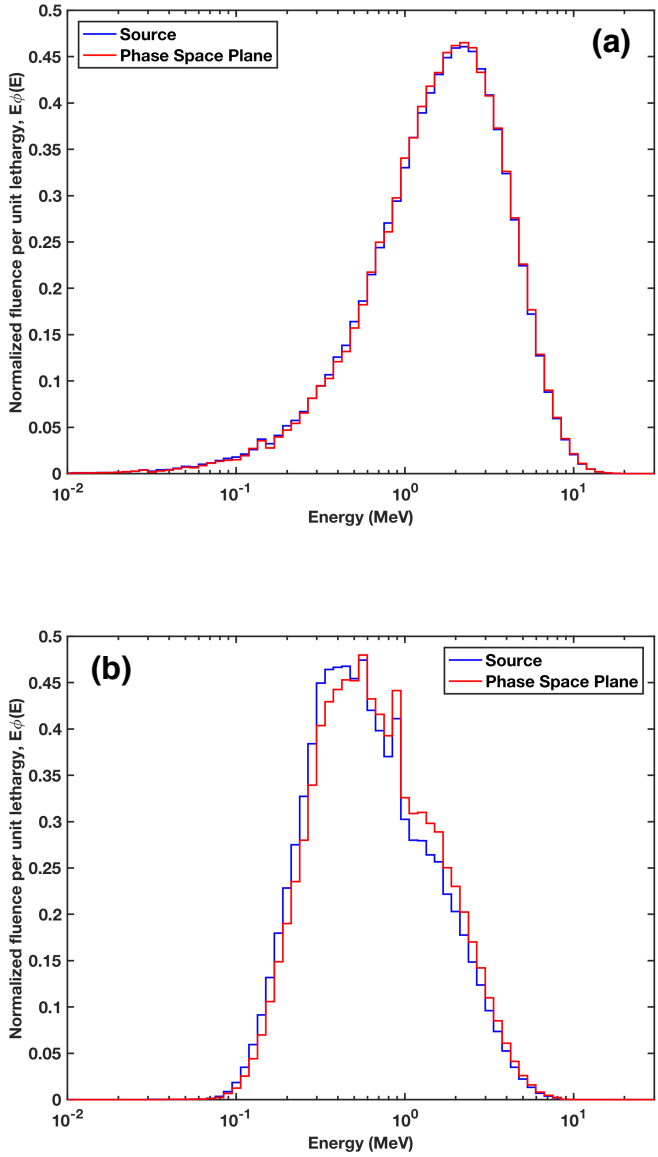

Figure 18. Comparison of the (a) neutron and (b) gamma spectra of the bare source (blue) with the spectra recorded on a 100 mm × 100 mm plane 80 mm away from the center of the source (red).

3.2.2.2. Microdosimetric Spectrum

The individual contributions of the gamma and neutron events from the experimental microdosimetric spectrum cannot be separated unless special extraction techniques are employed as described in the works of Colautti *et al* and Moro *et al* [32, 33]. In this study, to investigate the ionization events set in motion by gammas and neutrons, each of their contributions were scored separately in the MC simulation. The frequency weighted and dose weighted lineal energy distributions illustrating the separate gamma and neutron components are shown in figure 19(a) and (b), respectively.

Both spectra were obtained over a range of 0.01 keV/μm to 1000 keV/μm. The simulated frequency-mean ($\bar{y}_F$) and dose-mean ($\bar{y}_D$) lineal energies for the whole lineal energy range considered were 1.6 keV/μm and 52.0 keV/μm, respectively. According to the simulation results, gamma events constituted 94.8% of the total counts while neutron events comprised 5.2%. However, the largest fraction of the physical dose was due to neutron-induced depositions at 83% while gamma events only constituted 17%. Therefore, although gamma events dominated the depositions in the gas cavity, the greatest contribution to the dose were from high-LET particles set in motion by neutrons. This is reflected also in the shift of the $\bar{y}_D$ to a higher lineal energy value.

Based from the neutron simulation, photon induced events were observed to occur at event sizes less than 15.1 keV/μm. Similar behavior was observed in the previous section through the irradiation of the D60 TEPC with ^{137}Cs photon field wherein gamma events were found to mostly occur at low lineal energy

region. On the other hand, neutron events extended down to low lineal energy values, overlapping with the gamma contribution. This demonstrates that careful extraction must be employed in separating the neutron and gamma components when conducting experimental measurements. However, the extraction was not covered and performed in the present study.

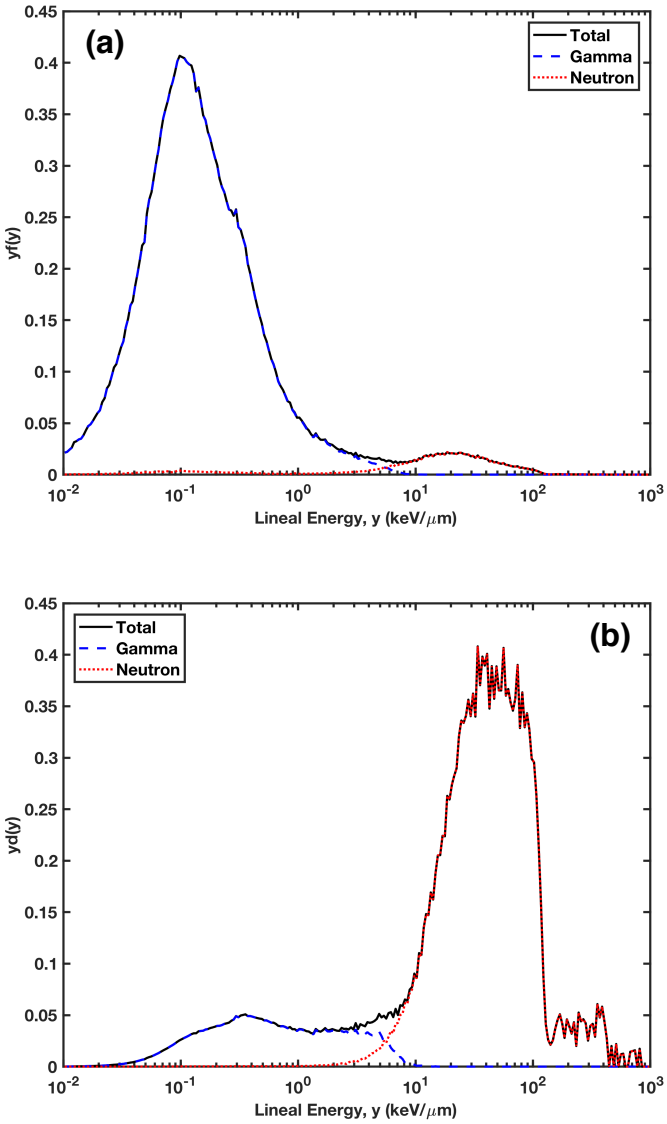

Figure 19. Simulated (a) $yf(y)$ and (b) $yd(y)$ distribution showing the separate contributions of the gamma (blue) and neutron (red) events.

3.2.3 Proton Edge Calibration

Figures 20 (a), (b), (c) and (d) represent the experimental proton edge region fitted at intervals 2000, 2500, 3000 and 3500 mV, respectively. The same fitting procedure was employed but at intervals 40, 50, 60 and 70 keV/μm for the simulated proton edge regions as shown in figures 21 (a), (b), (c) and (d), respectively. The resulting experimental and simulated proton edge markers, their averages and standard deviations are presented in tables 8 and 9, respectively.

For both the experiment and the simulation, $h_{\delta\delta}$ and its corresponding $y_{\delta\delta}$ showed the least deviation among the three proton edge markers. However, calibration using the h_{Flex} and y_{Flex} markers showed better agreement in the $yd(y)$ spectra and calculated $\bar{y}_F$ and $\bar{y}_D$ values. Therefore, the h_{Flex} and y_{Flex}were opted to be used in the re-calibration of the experimental data in terms of lineal energy given in equation 21. The resulting calibration factor was 0.0156 keV/μm per mV.

$$y_{calib(n)} = \frac{y_{Flex}}{h_{Flex}} = \frac{114.5\ keV/\mu m}{7363.8\ mV} = 0.0156\ keV/\mu m \cdot mV \qquad \textbf{Eq. 21}$$

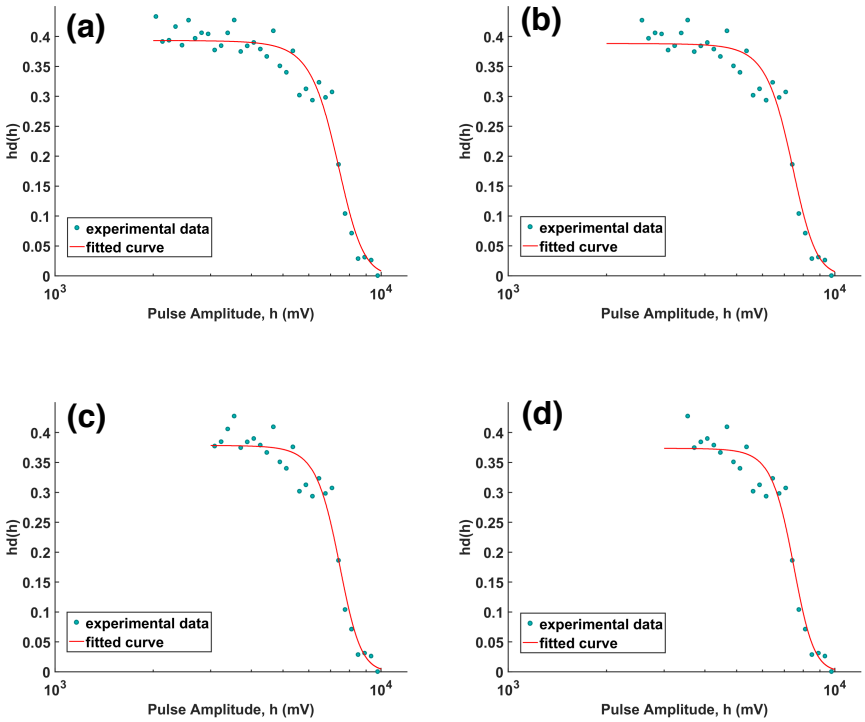

Figure 20. Fermi fit to the $hd(h)$ distribution at different pulse amplitude intervals starting from (a) 2000 mV, (b) 2500 mV, (c) 3000 mV and (d) 3500 mV.

Table 8. Experimental proton edge markers obtained at different pulse amplitude intervals for the neutron irradiation (unit: mV).

Interval	h_{Flex}	$h_{\delta\delta}$	y_{tC}
2000 ~ 9984.4	7305.9	8225.0	8701.9
2500 ~ 9984.4	7336.1	8209.2	8662.1
3000 ~ 9984.4	7393.6	8176.4	8582.5
3500 ~ 9984.4	7419.6	8160.7	8545.0
Average	**7363.8**	**8192.8**	**8622.9**
Standard Deviation	**52.0**	**29.5**	**71.8**

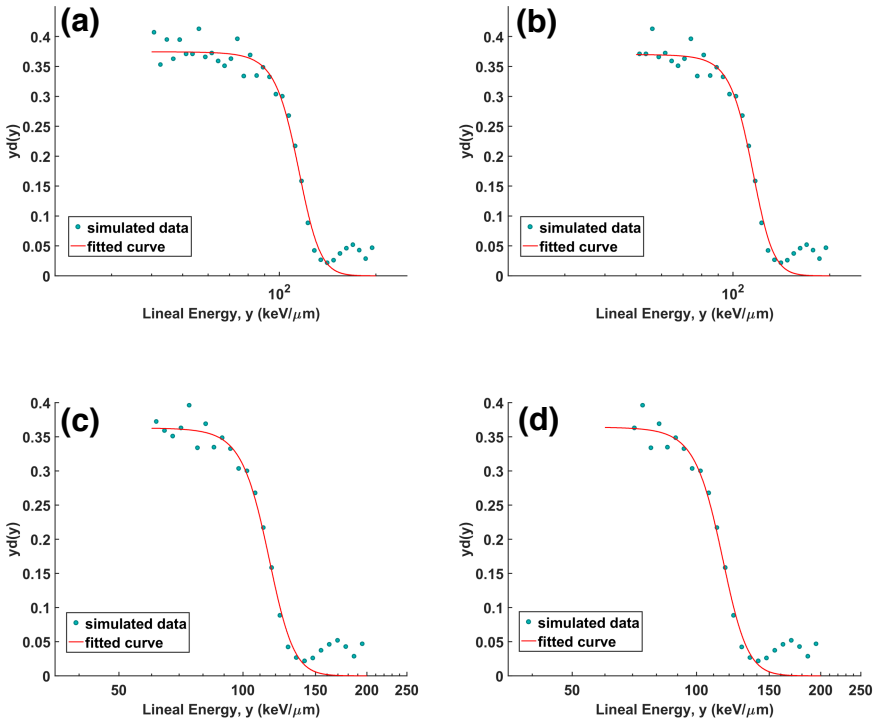

Figure 21. Fermi fit to the simulated $yd(y)$ distribution at different lineal energy intervals starting from (a) 40 keV/μm, (b) 50 keV/μm, (c) 60 keV/μm and (d) 70 keV/μm.

Table 9. Simulated proton edge markers obtained at different lineal energy intervals for the neutron irradiation (unit: keV/μm).

Interval	y_{Flex}	$y_{\delta\delta}$	y_{tC}
40 ~ 195	114.0	126.5	132.9
50 ~ 195	114.3	126.3	132.5
60 ~ 195	114.8	126.0	131.9
70 ~ 195	114.7	126.1	132.3
Average	**114.5**	**126.2**	**132.3**
Standard Deviation	**0.4**	**0.2**	**0.5**

3.2.4 Experiment and Simulation Comparison

Figure 22 shows the experimental and simulated $yd(y)$ distributions for the neutron measurement. The simulated spectra included high lineal energy depositions extending up to 700 keV/μm, beyond the detection range of the experimental set-up. However, the calibration resulted only to lineal energy depositions recorded from 0.17 keV/μm to 155.3 keV/μm for the experiment. Thus, the lineal energy contributions below and above these thresholds were disregarded in the simulation results to achieve a reasonable comparison between the measured and calculated spectra as shown in figure 23(a). The $\bar{y}_F$ and $\bar{y}_D$ values for both the simulation and experimental results (i.e., only contributions within the detection range) were also calculated and are presented in table 10.

Major discrepancies between the measured and simulated spectra can be observed particularly at lineal energies less than 10 keV/μm which were mostly due to gamma-induced events. It can also be observed that the peak between 10 keV/μm and 100 keV/μm of the simulated spectrum appears to be narrower and is slightly shifted to the right at high lineal energy values. Similar with the results from the photon measurements, underestimation of the experimental data in the region below 1 keV/μm was evident and removal of their contribution resulted in a better agreement between the experimental and simulated $yd(y)$ spectra as shown in figure 23(b). This also resulted in a drastic decrease in the percent difference in $\bar{y}_F$ from 97% to 15%. However, the difference in the $\bar{y}_D$ increased from 1.8% to 6.5%.

The lower measured values of $\bar{y}_F$ and $\bar{y}_D$ implies that more low-y events were recorded for the experiment which resulted to relatively lower average lineal energies for the frequency and dose distributions (i.e., $\bar{y}_F$ and $\bar{y}_D$, respectively). In order to verify that the origin of the discrepancies is associated to gamma-induced events, contributions of events less than 10 keV/μm were further removed. In doing so, an excellent agreement between the measured and calculated spectra was attained as presented in figure 23(c). This was also demonstrated in the lower discrepancies in the $\bar{y}_F$ and $\bar{y}_D$ values at 4.3% and 3.1%, respectively, as presented in table 10.

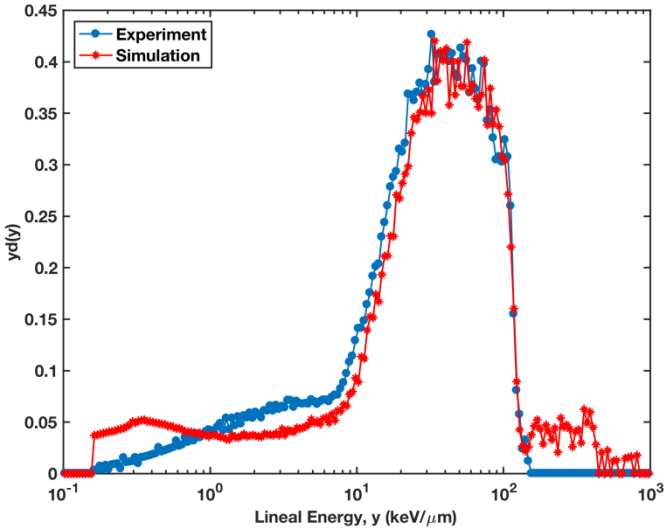

Figure 22. Comparison of the experimental $yd(y)$ distribution with the simulated $yd(y)$ distribution (calculated from 0.17 keV/μm to 1000 keV/μm).

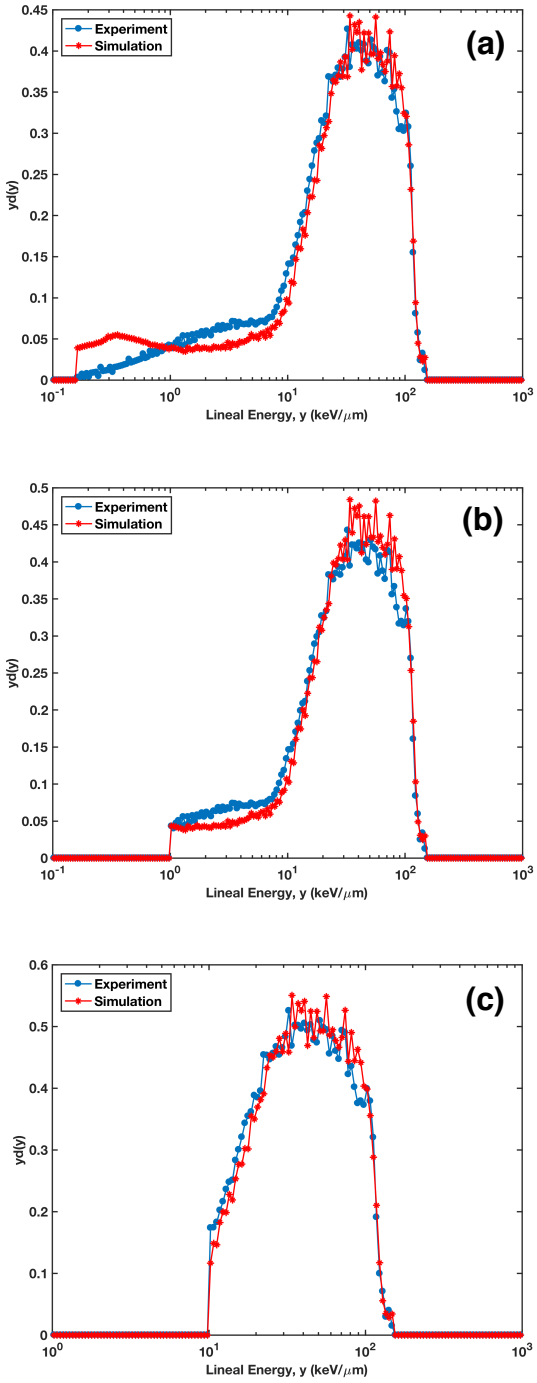

Figure 23. Comparison of the experimental and simulated $yd(y)$ spectra (a) for the whole detection range and reconstructed experimental and simulated $yd(y)$ spectra considering only contributions (b) above 1 keV/µm and (c) above 10 keV/µm for the neutron measurement.

Table 10. Frequency-mean ($\bar{y}_F$) and dose-mean ($\bar{y}_D$) lineal energy values for the whole and reconstructed (i.e., only contributions above 1 keV/μm and 10 keV/μm) spectra.

	$\bar{y}_F$ (keV/μm)			$\bar{y}_D$ (keV/μm)		
	Whole	y > 1	y > 10	Whole	y > 1	y >10
Experiment	6.5	12.5	31.4	38.9	40.4	47.1
Simulation	3.3	14.7	32.8	39.6	43.2	48.6
Percent Error (%)	97.0	15.0	4.3	1.8	6.5	3.1

An additional simulation was performed using the same set-up but implementing the *QGSP_BIC_HP_PEN* physics list. All elements in this physics list are the same with the previously used *QGSP_BIC_HP* physics list except that the electromagnetic physics was replaced with *G4EmPenelopePhysics* to allow transport of electrons down to 100 eV. Figures 24(a) and (b) illustrate the comparison between the experiment and the simulated $yd(y)$ distributions implementing the *G4EmStandardPhysics* (i.e., default electromagnetic physics list for QGSP_BIC_HP) and *G4EmPenelopePhysics* for the whole detection range and for the case considering only contributions above 1 keV/μm, respectively. The calculated $\bar{y}_F$ and $\bar{y}_D$ values for the distributions resulting from the Geant4-Penelope physics are likewise presented in table 11 along with the percent difference between the simulation and the experiment.

Aside from the noticeable peak at 0.39 keV/μm as shown in figure 24(a), the overall spectra acquired for both electromagnetic physics models were almost the same. This is more evident in figure 24(b) when lineal energy events less than 1 keV/μm were removed and the spectra were subsequently renormalized. In this region, the $\bar{y}_F$ values were found to not differ significantly with 14.7 keV/μm and 14.8 keV/μm for the standard and Penelope electromagnetic physics, respectively. Likewise, the $\bar{y}_D$ values were 43.2 keV/μm and 43.8 keV/μm, respectively.

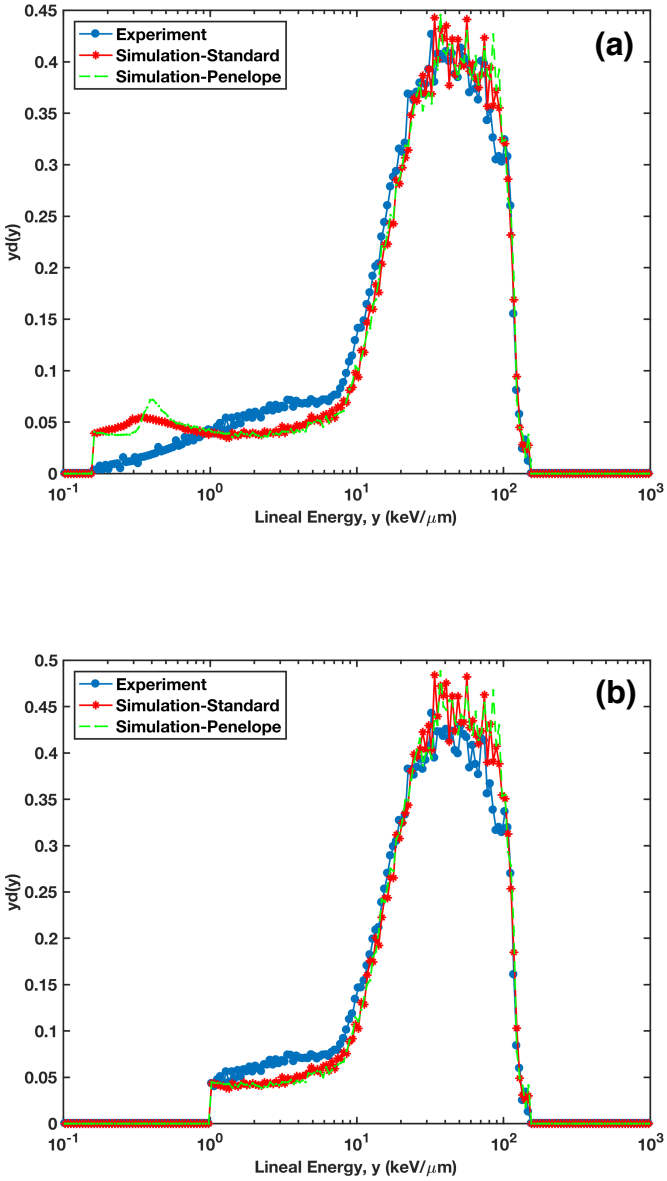

Figure 24. Comparison of the experimental (blue) and simulated $yd(y)$ spectra acquired using the *G4EmStandardPhysics* (red) and *G4EmPenelopePhysics* (green) (a) for the whole range and (b) considering only for contributions greater than 1 keV/μm obtained for the neutron measurement.

Table 11. Frequency-mean ($\bar{y}_F$) and dose-mean ($\bar{y}_D$) lineal energy values for the whole and reconstructed (only contributions above 1 keV/μm) spectra using *G4EmPenelopePhysics*.

	$\bar{y}_F$ (keV/μm)		$\bar{y}_D$ (keV/μm)	
	Whole	y > 1	Whole	y > 1
Experiment	6.5	12.5	38.9	40.4
Simulation (Penelope Physics)	3.3	14.8	40.0	43.8
Percent Error (%)	97.0	15.5	2.8	7.8

Discussion

Microdosimetric characterization for photon fields had been conducted in several previous works for both spherical [12] and cylindrical TEPCs [11, 34, 35] either to evaluate its performance when exposed to low LET fields or to use it for external calibration in the absence of an internal alpha calibration source. Similarly, in this study, the response of the D60 TEPC to a photon field was assessed by conducting experimental measurement and MC simulation using ^{137}Cs gamma source. Since an alpha calibration source was not available in this experimental set-up, self-calibration using the electron edge was employed for the gamma irradiation to relate the lineal energy to the channel numbers and to subsequently allow comparison between the experiment and the simulation results.

The obtained $yf(y)$ and $yd(y)$ distributions for the gamma irradiation showed low lineal energy depositions up to 12.6 keV/μm which is a characteristic behavior of photon fields [34]. The microdosimetric distributions obtained in this study exhibited similar trend and shape with the measured and calculated microdosimetric spectra for ^{137}Cs reported in the works of Moro *et al* and Rollet *et al* [12, 35]. However, it is difficult to make a direct comparison with these previous studies regarding TEPC measurements using ^{137}Cs because different gas cavity geometry, type of detection gas and simulated site sizes were used which affects the position of the electron edge.

The experimental $yd(y)$ spectrum showed a better agreement with the

calculated spectrum when lineal energy deposition events below 1 keV/μm were removed. The discrepancies at y < 1 keV/μm can be attributed to the detection limitations of the TEPC as the preamplifier was slightly separated from the detector which creates a lot of noise. This makes it difficult to distinguish comparatively low lineal energy depositions from noise and thus, resulting for some of these events to be filtered out and eliminated through electronic discrimination. Further optimization in the design of the D60 TEPC is needed to improve the detection energy resolution.

TEPCs have also been widely used in mixed field dosimetry not only because of its excellent neutron and gamma discrimination but also because of its ability to physically allow examination of the patterns of energy depositions in the microscopic level, similar to the dimensions of cellular and subcellular structures [1, 36]. Such measurements are of extreme importance particularly in the characterization of mixed radiation fields because the spatial distribution of energy deposition is critical in understanding the mechanism of radiation damage [2]. As a result, numerous extensive research on the characterization of TEPCs when exposed to neutron [7, 32] and proton fields [2, 6, 37] have been carried out in the past associated primarily to the increase in the popularity of alternative radiation therapy modalities such as proton and boron neutron capture therapies.

Since the D60 TEPC was developed and fabricated for the purpose of neutron monitoring, irradiations with ^{252}Cf neutron field coupled with MC simulations were also performed in this study. As illustrated in figure 23(a), the comparison of the experimental data with the simulation results showed significant

differences especially in the low lineal energy region (i.e., y < 10 keV/μm). Experimental results were underestimated mainly in the region less than 1 keV/μm due to difficulty in resolving energy depositions experimentally which was also observed in the gamma measurements. Elimination of their contribution resulted in a better correspondence in the experimental and simulated $yd(y)$ spectra especially in the region of the neutron-induced peak mainly found at lineal energies greater than 15.5 keV/μm. However, underestimation of events for the simulated spectra below 15.5 keV/μm was evident as shown in figure 23(b).

Further removal of events less than 10 keV/μm demonstrated excellent agreement between the experiment and simulation resulting to uncertainties in the $\bar{y}_F$ and $\bar{y}_D$ values within 5%. This indicated that the disagreement between the measured and calculated $yd(y)$ spectra originated mostly from the region less than 10 keV/μm which are dominated by photon-induced events. Since equal areas correspond to equal fractions of imparted dose in the microdosimetric spectrum, the underestimation in the low LET region led to an increase in the fraction of contribution of high LET events as illustrated in figure 23(b).

In order to eliminate the discrepancies in the lower lineal energy region, additional simulation implementing a different electromagnetic physics model was performed. Previous studies regarding TEPC simulation indicated that the primary reasons of the difference in the low-LET region were the ability of the model to produce delta electrons and the electron transport threshold of the simulation program [38, 39]. In this study, the default electromagnetic physics,

G4EmStandardPhysics, in the QGSP_BIC_HP physics list was implemented in the calculations. This model uses the default transport threshold of 990 eV wherein below this energy, no further secondary particles were produced. This limitation of our model may have resulted in approximations on the energy depositions in the TEPC. Therefore, instead of the *G4EmStandardPhysics*, the *G4EmPenelopePhysics* was implemented to model electromagnetic interactions down to 100 eV in order to further improve the accuracy of the simulation results. However, although a small peak occurred at 0.39 keV/μm as illustrated in figure 24(a), this did not induce a significant change in the spectrum. As shown in figure 24(b), the simulated $yd(y)$ distributions considering only depositions with y > 1 keV/μm obtained for both the Standard and Penelope physics remained almost the same. A significant change in the $\bar{y}_F$ and $\bar{y}_D$ values calculated using the *G4EmPenelopePhysics* was also not observed as indicated in table 11. Therefore, it can be concluded that there is no need to implement the *G4EmPenelopePhysics* in the TEPC simulations as it only increases the calculation time from 3 hours to 10 hours using 32 Intel Xeon E5-2680 CPUs (2.70 GHz, 8 cores, 2 threads per core) but does not introduce improvements in the microdosimetric spectra.

It also has to be pointed out that the simulation was performed without consideration of other scattering structures surrounding the TEPC like the table or the walls and thus, additional contributions from the scattered radiation were omitted which may have been a crucial factor. However, it is not clear whether these structures caused the difference and further investigation on this matter is required. The discrepancies between the simulation and the experimental

results suggest that room for improvements in the simulation model and experimental set-up are needed. Nonetheless, the results showed that the general trend of the experimental distribution was reproduced reasonably well by the simulation model.

Another limitation of this work is that the experimental set-up for the neutron measurement permitted a maximum detectable lineal energy of 155.3 keV/μm. As demonstrated from figure 22, events up to 700 keV/μm were recorded which is why acquisition of the overall microdosimetric spectra for neutron irradiation is usually conducted using three different amplifier gains to cover all low- and high-LET radiation events [25, 32, 40]. However, the acquisition of the spectra for the neutron measurements in the present work was done using single gain mode only and thus, only a tiny peak after the proton edge was visible. This portion is part of the third peak typical from neutron irradiations which are primarily due to depositions from alpha particles and heavy ions.

Finally, over the detection range considered for the photon and neutron irradiations, the measured physical absorbed doses were 6.19 μGy and 9.23 μGy, respectively. The corresponding dose equivalent calculated using equation 17 for the gamma and neutron measurements were 6.20 μSv and 95.54 μSv, respectively. For the gamma case, the absorbed dose and dose equivalent were found to be almost the same as the majority of the depositions lie below 10 keV/μm where the Q is 1. However, a drastic increase in the dose equivalent by a factor of 10 was observed for the neutron measurements owing to the presence of high LET events mostly from neutron interactions.

Conclusions

The microdosimetric characterization of the D60 TEPC was carried out for photon and neutron fields through experimental measurements and MC simulations. The microdosimetric spectrum obtained from exposure to ^{137}Cs showed a satisfactory agreement with the simulations for lineal energies (y) over 1 keV/μm. On the other hand, the measured microdosimetric spectrum for a ^{252}Cf neutron source agreed fairly well with the calculated spectra especially in the region of the neutron-induced peak (y > 10 keV/μm). Along the regions above 1 keV/μm for photon and 10 keV/μm for neutron irradiations, the differences between the measured and calculated $\bar{y}_F$ and $\bar{y}_D$ values were less than 5%. These results indicate that Geant4 can reproduce the measured microdosimetric spectra with reasonable accuracy when low lineal energy events, which cannot be measured accurately due to the electronic noise, were excluded. Finally, the validation of the simulation model with the experimental findings in this work would be extremely valuable for our future goal of designing and developing mini-TEPCs tailored for BNCT dosimetry.

References

1. Rossi, H.H. and M. Zaider, *Microdosimetry and its applications*. 1996, New York: Springer. xii, 321 p.
2. Pan, C.Y., et al., *Microdosimetry spectra and relative biological effectiveness of 15 and 30MeV proton beams.* Appl Radiat Isot, 2015. **97**: p. 101-105.
3. International Commission on Radiation Units and Measurements., *Microdosimetry*. ICRU Report 36. 1983, Bethesda, Md., U.S.A.: International Commission on Radiation Units and Measurements. ix, 118 p.
4. Hugtenburg, R.P., *Monte Carlo modelling of acute and late effects in radiation therapy.* Appl Radiat Isot, 2012. **70**(7): p. 1113-7.
5. Cesari, V., Iborra, N., De Nardo, L., Querini, P., Conte, V., Colautti, P., Tornielli, G., Chauvel, P., *Microdosimetric Measurements of the Nice Therapeutic Proton Beam.* Physica Medicina, 2001. **XVII**: p. 76-82.
6. De Nardo, L., et al., *Mini-TEPCs for radiation therapy.* Radiat Prot Dosimetry, 2004. **108**(4): p. 345-52.
7. Moro, D., et al., *BNCT dosimetry performed with a mini twin tissue-equivalent proportional counters (TEPC).* Appl Radiat Isot, 2009. **67**(7-8 Suppl): p. S171-4.
8. Moro, D. and S. Chiriotti, *EuTEPC: measurements in gamma and neutron fields.* Radiat Prot Dosimetry, 2015. **166**(1-4): p. 266-70.
9. Nam, U.-W., et al., *Development and Characterization of Tissue Equivalent Proportional Counter for Radiation Monitoring in International Space Station.* Journal of Astronomy and Space Sciences, 2013. **30**(2): p. 107-112.
10. Chiriotti, S., et al., *Equivalence of pure propane and propane TE gases for microdosimetric measurements.* Radiat Prot Dosimetry, 2015. **166**(1-4): p. 242-6.
11. Conte, V., Moro, D., Grosswendt, B., Colautti, P., *Lineal energy calibration of mini tissue-equivalent gas-proportional counters (TEPC).* AIP Conference Proceedings, 2013. **1530**(1): p. 171-178.

12. Moro, D., et al., *Lineal energy calibration of a spherical TEPC.* Radiat Prot Dosimetry, 2015. **166**(1-4): p. 233-7.

13. Crossman, J.S.P. and D.E. Watt, *Inherent Calibration of Microdosemeters for Dose Distribution in Lineal Energy.* Radiation Protection Dosimetry, 1994. **55**(4): p. 295-298.

14. Cesari, V., et al., *Nanodosimetric measurements with an avalanche confinement TEPC.* Radiat Prot Dosimetry, 2002. **99**(1-4): p. 337-42.

15. Agostinelli, S., et al., *Geant4—a simulation toolkit.* Nuclear Instruments and Methods in Physics Research Section A: Accelerators, Spectrometers, Detectors and Associated Equipment, 2003. **506**(3): p. 250-303.

16. Kellerer, A.M., *2 - Fundamentals of Microdosimetry*, in *The Dosimetry of Ionizing Radiation*, K.R. Kase, B.E. BjÄRngard, and F.H. Attix, Editors. 1985, Academic Press. p. 77-162.

17. B. Firestone, R., S. Y. Frank Chu, and C. M. Baglin, *8th edition of the Table of Isotopes: 1998 Update*. Vol. -1. 1997.

18. Browne, E., R. Firestone, and V.S. Shirley, *Table of Radioactive Isotopes*. 1986.

19. Radev, R. and T. McLean, *Neutron Sources for Standard-Based Testing*, in *LLNL-TR-664160.* 2014, Lawrence Livermore National Lab. (LLNL), Livermore, CA (United States). p. 12 p.

20. Verbinski, V.V., H. Weber, and R.E. Sund, *Prompt Gamma Rays from 235U(n,f), 239Pu(n,f), and Spontaneous Fission of 252Cf.* Physical Review C, 1973. **7**(3): p. 1173-1185.

21. Fröhner, F.H., *Evaluation of 252Cf Prompt Fission Neutron Data from 0 to 20 MeV by Watt Spectrum Fit.* Nuclear Science and Engineering, 1990. **106**(3): p. 345-352.

22. Martin, R.C., J.B. Knauer, and P.A. Balo, *Production, distribution and applications of californium-252 neutron sources.* Applied Radiation and Isotopes, 2000. **53**(4): p. 785-792.

23. Al-Bayati, S., *The Application of Experimental Microdosimetry to Mixed-Field Neutron-Gamma Dosimetry*. 2012, University of Ontario Institute of

Technology: Ontario, Canada.

24. Ali, F., *Design and Characterization of Next-Generation Tissue Equivalent Proportional Counters for Use in Low Energy Neutron Fields.* 2014, University of Ontario Institute of Technology: Ontario, Canada.

25. Motisi, E., *Development of Microdosimetric Techniques Applied to Hadron Therapy*. 2015, University of Padua: Padua, Italy.

26. Verbeke, J., C. Hagmann, and D. Wright, *Simulation of Neutron and Gamma Ray Emission from Fission and Photofission*. UCRL-AR-228518-REV-1. 2016: Lawrence Livermore National Laboratory.

27. Lestone, J., *Watt parameters for the Los Alamos Model : Subroutine getab*. LA-UR-07-6090 2007: Los Alamos National Laboratory.

28. Tan, J. and J. Bendahan, *Geant4 Modifications for Accurate Fission Simulations.* Physics Procedia, 2017. **90**: p. 256-265.

29. B., S.J., et al., *Composition of A-150 tissue-equivalent plastic.* Medical Physics, 1977. **4**(1): p. 74-77.

30. International Commission on Radiological Protection., *1990 recommendations of the International Commission Radiological Protection : adopted by the Commission in November 1990*. 1st ed. ICRP Publication 60. 1991, Oxford, England ; New York: Published for the Commission by Pergamon. vii, 201 p.

31. Valentine, T.E., *Evaluation of prompt fission gamma rays for use in simulating nuclear safeguard measurements.* Annals of Nuclear Energy, 2001. **28**(3): p. 191-201.

32. Colautti, P., et al., *Microdosimetric measurements in the thermal neutron irradiation facility of LENA reactor.* Appl Radiat Isot, 2014. **88**: p. 147-52.

33. Moro, D., Seravalli, E., Colautti, P., *Statistical and Overall Uncertainties in BNCT Microdosimetric Measurements*, in *LNL-INFN(REP)199/2003*. 2003, Legnaro National Laboratories, Italian Institute of Nuclear Physics.

34. Bortot, D., et al., *A novel avalanche-confinement TEPC for microdosimetry at nanometric level.* Radiation Measurements, 2017. **103**: p. 1-12.

35. Rollet, S., et al., *Monte Carlo simulation of mini TEPC microdosimetric spectra: Influence of low energy electrons.* Radiation Measurements, 2010. **45**(10): p. 1330-1333.

36. Nikjoo, H., et al., *Modelling and calculations of the response of tissue equivalent proportional counter to charged particles.* Radiation Protection Dosimetry, 2007. **126**(1-4): p. 512-518.

37. Chiriotti, S., et al., *Microdosimetric Measurement of Secondary Radiation in the Passive Scattered Proton Therapy Room of iThemba LABS Using a Tissue-Equivalent Proportional Counter.* Radiation Protection Dosimetry, 2018: p. ncy056-ncy056.

38. Burigo, L., et al., *Microdosimetry of radiation field from a therapeutic 12C beam in water: A study with Geant4 toolkit.* Nuclear Instruments and Methods in Physics Research Section B: Beam Interactions with Materials and Atoms, 2013. **310**: p. 37-53.

39. Mazzucconi, D., et al., *Monte Carlo simulation of a new TEPC for microdosimetry at nanometric level: Response against a carbon ion beam.* Radiation Measurements, 2018. **113**: p. 7-13.

40. Cho, I.C., et al., *Microdosimetry measurements for low-energy particles using a mini TEPC with removable plug.* Radiation Physics and Chemistry, 2017. **137**: p. 83-87.

Abstract (in Korean)

국 문 초 록

조직등가 비례 계수기 (TEPC)는 미시적 선량을 측정할 때 일반적으로 사용되는 방사선 검출기다. 조직 등가 비례 계수기는 저압 기체로 채워진 공간에 흡수된 에너지를 측정함으로써 미세선량을 얻을 수 있다. 또한, 특히 세포의 민감한 구조에 방사선 손상 메커니즘을 이해하는 데 중요한 미시적인 에너지 분포 패턴의 거동을 관찰할 수 있게 한다. 지난 20년 동안, 우주 탐사에 대한 관심이 증가하고 중입자 방사선 치료법도 가능해졌기 때문에 이러한 환경에서 여러 종류의 방사선 선량을 측정하기 위해서 다양한 모양과 크기의 TEPC가 개발되었다.

본 학위논문의 목적은 한국 천문 연구원 (KASI)이 개발한 Benjamin 류의 TEPC의 감마선원 및 중성자원에 대한 반응을 관찰하는 것이다. Cs-137 감마 및 Cf-252 중성자 선원에 노출되었을 때 2 μm 사이트의 에너지 흡수량 측정 능력을 평가하기 위해서 실험을 수행하였다. 또한, 실험 결과를 검증하기 위해서 Geant4를 이용한 TEPC의 몬테카를로 모델링을 수행하였다.

Frequency-weighted 선형 에너지와 dose-weighted 선형 에너지 스펙트럼을 실험과 전산모사로 획득하고 각각의 frequency mean 선형 에너지 ($\bar{y}_F$)와 dose mean 선형 에너지($\bar{y}_D$)를 계산하였다. 낮은 선형 에너지 이벤트가 무시될 때 시뮬레이션과 실험으로 얻어진 $\bar{y}_F$ 및 $\bar{y}_D$의 차이는 감마 선원에 노출의 경우 각각 2.8% 및 4%이였다.

중성자의 경우에는 특히 중성자가 유도된 피크에 계산된 스펙트럼은 실험 결과와 전반적으로 양호한 일치를 갖는 것으로 관찰되었다. 그러

나, 낮은 선형 에너지 영역을 따라 시뮬레이션 스펙트럼의 과소 평가가 관찰되었다. 감마 영역을 제거하면 측정 및 계산된 $\bar{y}_F$ 및 $\bar{y}_D$ 값의 차이는 5%이내였다. 중성자의 경우 약간의 차이가 있었지만 Geant4를 이용한 시뮬레이션은 두 개 모두의 방사선환경에서 실험상의 미세선량 스펙트럼을 합리적이고 성공적으로 예측 및 재현할 수 있었다.

주요어: 조직등가 비례 계수기, 선형 에너지, 미시적 선량측정, 광자, 중성자

학번: 2016-27697